Mechanism Clarification of Coming out of the Shaft from Shrink-Fitted Ceramic Sleeve Roller under Bending Load Focusing on the Driving out Force

	Zhang　Guowei
	17104　　479
URL	http://hdl.handle.net/10228/00007803

Mechanism Clarification of Coming out of the Shaft from Shrink-Fitted Ceramic Sleeve Roller under Bending Load Focusing on the Driving out Force

By

Guowei Zhang

Department of Mechanical Engineering

Kyushu Institute of Technology

Acknowledgments

My study at Kyushu Institute of Technology will soon come to an end, and at the completion of my graduation thesis, I wish to express my sincere appreciation to all those who have offered me invaluable help during the four years of my doctoral term.

Firstly, I would like to express my heartfelt gratitude to my supervisor, Professor Nao-Aki Noda, for his constant encouragement and guidance. He has walked me through all the stages of the writing of this thesis. I was first introduced to the study in Japan when professor Noda asked my supervisor Xuehong HE whether some student is willing to further his/her study as a doctoral student during my master term. Then he helped me with the application of MEXT scholarship, which supported my study in Japan for 4 years. Without his consistent and illuminating instruction and enthusiastic help, this thesis could not have reached its present form.

Secondly, I am also greatly indebted to my lab Advisor Yoshikazu SANO, who has been supporting my research and Japanese study as well as my tough life with patience and kindness.

Thirdly, I am also greatly indebted to Dr. Yasushi Takase, who has been supporting my study with patience and kindness since I entered KIT in September of 2015.

My supervisor, Professor Xuehong He in Northeastern University (China), introduced me to the study in Japan, and helped me in the application of scholarship. I would like to give my thanks to her for all her contribution and encouragement during my toughest period. Under her encouragement, I was able to constantly broaden my horizons, she also gave me a lot of research and life guidance. It was she who encouraged me to learn Japanese that enabled me to practice oral writing unremittingly, pass the Japanese N1 test, and make great progress in oral Japanese. I am also indebted to her for his

constructive comments on my career.

I also owe my sincere gratitude to my friends and my fellow collaborators who gave me their time in helping me work out my problems during the difficult course of the thesis, especially to Mr. Hiromasa Sakai, Mr. Shun Oshiro, who helped me with the translation of Japanese.

My thanks would go to my beloved parents, for their loving considerations and great confidence in me all through these years. Without the encouragement of my father, I would not have been abroad seeking for more knowledge. I feel very lucky that I also have a great mother. It's not easy for her to live alone during my doctoral study period, who has supported me all the time. My elder brother is very wise, he also supported me all the time. And I would like to give my wife, Mrs. Mengdi Qiao, many thanks for her support and encouragement. Without her companion, I'm not sure I could have the courage to face the difficulty in my study. Especially she gave me a large amount of spiritual support and encouragement for my Japanese study and research.

Finally, the financial support of MEXT scholarship of Japanese government, which made it possible for my study in Japan, is gratefully acknowledged.

Abstract

Ceramic sleeve rollers have been developed recently to be used in steel manufacturing industries efficiently. Ceramics have high corrosion resistance, high heat resistance and high wear resistance. The ceramic cylinder and the steel shafts of both ends are joined together to form the ceramic sleeve roller. It is found that the shrink fitting method is the most suitable connecting method for the roller. However, since only small shrink fitting ratios can be applied due to the brittleness of the ceramics, coming out of the shaft from the sleeve was reported during repeated loadings.

This new failure should be analyzed and prevented. Previously, the finite element method was used to analyze the coming out behavior. Then, the roller rotation was replaced by the load shifting on the fixed roller by the finite element method. Since the calculation time was very enormous, only few rotation cycles were conducted. To realize much more number of loading cycles to investigate the coming out mechanism, therefore, a two-dimensional simulation was conducted to reduce the calculation time and more than $N = 40$ cycles were investigated. Those studies have proved that the coming out behavior can be numerically realized on the two-dimensional and three-dimensional simulations, while few studies have been focused on clarifying the coming out mechanism and analyzing the driving out force generated on the shaft, which is also very important for the future design of the roller without coming out. This thesis is composed of total of 5 chapters and organized as follows.

Chapter 1 gives an introduction of the coming out problem of the shaft from the ceramic sleeve and the finite element method. Also gives an overview of previous studies on the coming out phenomenon. Then research purpose of this thesis is introduced, focusing on clarification of the coming out mechanism of the shaft from the ceramic sleeve and analysis of the driving out force generated on the shaft under bending load.

In Chapter 2, to find out the coming out mechanism of the shaft from the sleeve with less

computational time in a much more understandable way, a simplified two-dimensional model with a newly designed stopper is used to investigate the coming out mechanism. The two-dimensional shrink-fitted structure is considered by replacing the shaft with the inner plate and by replacing the sleeve with the outer plate. The inner plate gradually comes out until it is stopped by the stopper under the standard simulation condition. This is because driving out force F_d is generated on the inner plate when the alternate load is applied and drives the shaft out gradually. Then the generation mechanism of driving out force is clarified with the help of the stopper. And F_d is also calculated. It is essential to calculate out the driving out force F_d to guide the design of the real model for the future study. Finally, the process of coming out is explained in terms of the residual displacement based on the deformation and the displacement of the inner plate (shaft) under a new loading method.

In Chapter 3, before investigating the effects of the design factors on the driving out force by an actual three-dimensional model, it is useful to perform the analysis by a two-dimensional model. The effect of the shrink fitting ratio δ/d on the driving out force F_d of the inner plate (shaft) is investigated and discussed as well as several other parameters, such as load P, friction coefficient μ, shrink fitting ratio δ/d, shrink fitting length l, Young's modulus of the inner plate (shaft) E_{in}. When designing an actual three-dimensional roller, it is sufficient to find the maximum value of the driving out force F_d and based on this value for the strength design of the structure for prevention of the coming out phenomenon.

In Chapter 4, the actual three-dimensional model is considered to explore the coming out mechanism and to calculate the driving out force F_d^{3D}. Here, a novel Ball-stopper installed outside of the shaft designed for the three-dimensional model originally fertilising the analysis of the generation mechanism of driving out force F_d^{3D} and the calculation of F_d^{3D} is introduced. The function of this kind of Ball-stopper is firstly proved by comparing with the two-dimensional model with an inner stopper used in Chapter 2 and Chapter 3. Then the generation mechanism of driving out force F_d^{3D} is clarified and F_d^{3D} is calculated out with the help of the Ball-stopper.

Finally, Chapter 5 provides the major conclusions, the most significant outcomes and contributions and suggestions for future works.

Contents

List of tables

List of figures

Nomenclature

P	Bending load of two-dimensional model [N]
P_{upward}	Upward bending load applied to the two-dimensional model [N]
P_{upward}	Downward bending load applied to the two-dimensional model [N]
H	Height of the inner stopper of the two-dimensional model [mm]
N	Cycle number of the load
N_c	Cycle number when the inner plate starts to contact with the outer plate
μ	Friction coefficient
l	Shrink fitting length
δ/d	Shrink fitting ratio
v	Poisson's ratio
E	Young's modulus
l/d	Fitted length ratio
E_{in}	Young's modulus of the inner plate
E_{in}^{In}	The filler part's Young's modulus of the inner plate
E_{in}^{Out}	The steel part's Young's modulus of the inner plate
F_d	Driving out force generated on the inner plate [N]
F_d^{3D}	Driving out force generated on the shaft (three-dimensional model) [N]
$F_\tau^{resultant}$	The resultant frictional shear force generated on the surface of the shaft
F_s	Contact force between the inner plate and the stopper
F_τ^{up}	Shear stress distributed on the upside of the inner plate
F_τ^{down}	Shear stress distributed on the downside of the inner plate

l_c^{up} Contact length of the upside of the inner plate with the outer plate

l_c^{down} Contact length of the downside of the inner plate with the outer plate

l_{gap} Length of the gap of the inner stopper installed on the outer plate

u_{xD} Displacement of the Point D of the inner stopper

Chapter 1 Introduction

1.1 Research Backgrounds

Recently, ceramic is widely used for large structural because of outstanding properties such as high wear resistance, high corrosion resistance, and high temperature resistance. In this study, the ceramic roller is considered to be used in the furnace whose temperature is more than 1,000℃. Here, the roller consisting of ceramics sleeve is connected to the steel shaft.

Advanced ceramics (see Appendix A & B) has attracted attention in wide engineering fields in the last five decades [1-4] because ceramic has some advantageous properties mentioned above [5]. The usage of advanced ceramic for engineering applications has been promoted since 1970s as electrical insulator [4], automotive engines [6-10], tribology components [11, 12], cylinder head plates, pistons and turbocharger rotors [13, 14], gas turbine engines [15, 16], machine tools [17], hot rolling mills and low-pressure die casting machine. However, under both thermal and mechanical loadings, structural ceramic is not very popular until now compared to functional ceramic widely used [18].

As an example, intense efforts have been done to develop ceramic gas turbine during 1950s-1990s [15, 16], but only ceramic coatings are in use now. This is because all ceramic components may be too brittle to design turbine component. Generally speaking, the manufacturing and processing technologies of advanced ceramic have progressed very relatively slowly.

In recent years, advanced ceramic applications subjected to thermal and mechanical loads have been studied by several authors. Study on treatment of molten metal, ceramic die cast sleeves and ceramic stalks in the low-pressure die casting machine have been successfully performed [19-22]. Similar ceramic structures under a high-temperature environment in continuous galvanizing line [23, 24], in the continuous pickling line [25, 26], and the heating furnace [27] have also been considered.

In this thesis, I will focus on hearth rollers used in the heating furnace as is shown in Figure 1.1 whose atmosphere temperature is more than 1000℃. Conventional rollers have ceramic coated steel sleeve and shafts connected each other by shrink fitting. Although the inside of the roller is cooled by water circulation to reduce the temperature, the roller coating deteriorates in a short period due

to the thermal expansion difference between ceramic and steel. Then, finally, the conventional rollers are changed very frequently because of the wear induced by the hot conveyed strips. Therefore, a new roller consisting of the ceramic sleeve and steel shafts at both ends will be considered as is illustrated in Figure 1.2. All ceramics sleeve may prevent most of the defects observed at coated ceramic, which can extend the roller life. In this study, the finite element method is used to simulate and analyze the behavior of the roller.

The finite element method is a numerical method for solving problems of engineering and mathematical physics. It has become a practical one for solving engineering problems only in the past 62 years (paralleling the developments associated with the modern high-speed electronic digital computer). Typical problem areas of interest in engineering and mathematical physics that are solvable by use of the finite element method include structural analysis, heat transfer, fluid flow, mass transport, and electromagnetic potential. Analytical solutions are those given by a mathematical expression that yields the values of the desired unknown quantities at any location in a body here total structure or
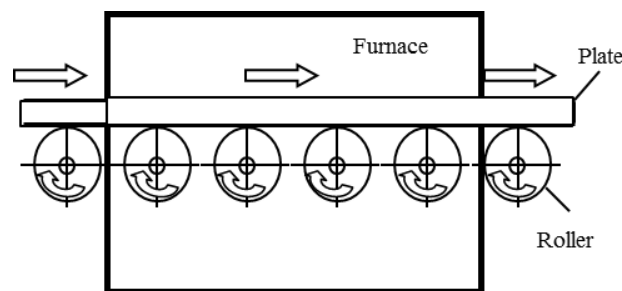
Figure 1.1 Layout of rollers in heating furnace
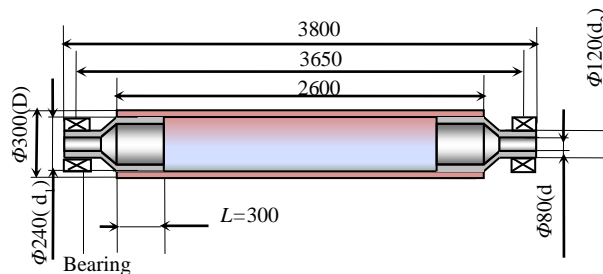
Figure 1.2 Structure and dimensions of a real ceramic roller model (mm) (3D)

the physical system of interest) and are thus valid for an infinite number of locations in the body.

In this thesis, the finite element method is mainly used to perform lots of numerical simulation calculation conveniently with much less cost especially for some large structures under complicated environmental load which is extremely difficult to perform a test. It can provide us with useful calculation results for strength analysis, special mechanics behavior analysis, structure design and so on.

The modern development of the finite element method began in the 1940s in the field of structural engineering with the work by Hrennikoff [29] in 1941 and McHenry [30] in 1943, who used a lattice of line (one-dimensional) elements (bars and beams) for the solution of stresses in continuous solids.

The first treatment of two-dimensional elements was by Turner et al. [31] in 1956. They derived stiffness matrices for truss elements, beam elements, and two-dimensional triangular and rectangular elements in plane stress and outlined the procedure commonly known as the direct stiffness method for obtaining the total structure stiffness matrix. From the early 1950s to the present, enormous advances have been made in the application of the finite element method to solve complicated engineering problems.

The finite element method can be used to analyze both structural and nonstructural problems. In this thesis, structural areas are mainly focused on. Typical structural areas include :

1. Stress analysis, including truss and frame analysis (such as pedestrian walk bridges, high rise building frames, and windmill towers), and stress concentration problems, typically associated with holes, fillets, or other changes in geometry in a body (such as automotive parts, pressures vessels, medical devices, aircraft, and sports equipment).

2. Buckling, such as in columns, frames, and vessels.

3. Vibration analysis, such as in vibratory equipment.

4. Impact problems, including crash analysis of vehicles, projectile impact, and bodies falling and impacting objects.

Nonstructural problems include:

1. Heat transfer, such as in electronic devices emitting heat as in a personal computer microprocessor chip, engines, and cooling fins in radiators.

2. Fluid flow, including seepage through porous media (such as water seeping through earthen dams), cooling ponds, and in air ventilation systems as used in sports arenas, etc., air flow around racing cars, yachting boats, and surfboards, etc.

3. Distribution of electric or magnetic potential, such as in antennas and transistors Finally, some biomechanical engineering problems (which may include stress analysis) typically include analyses of the human spine, skull, hip joints, jaw/gum tooth implants, heart, and eye.

Here, some typical applications on structural areas of the finite element method will be presented. These applications will illustrate the variety, size, and complexity of problems that can be solved using the method and the typical discretization process and kinds of elements used. A problem of the hydraulic cylinder rod end shown in Figure 1.3, was modeled by 120 nodes and 297 plane strain triangular elements. Symmetry was also applied to the whole rod end so that only half of the rod end had to be analyzed. The purpose of this analysis was to locate areas of high stress concentration in the rod end.

Figure 1.4 illustrates the use of a three-dimensional solid element to model a swing casting for a backhoe frame. The three-dimensional hexahedral elements are necessary to model the irregularly shaped three-dimensional casting. Two-dimensional models certainly would not yield accurate engineering solutions to this problem.
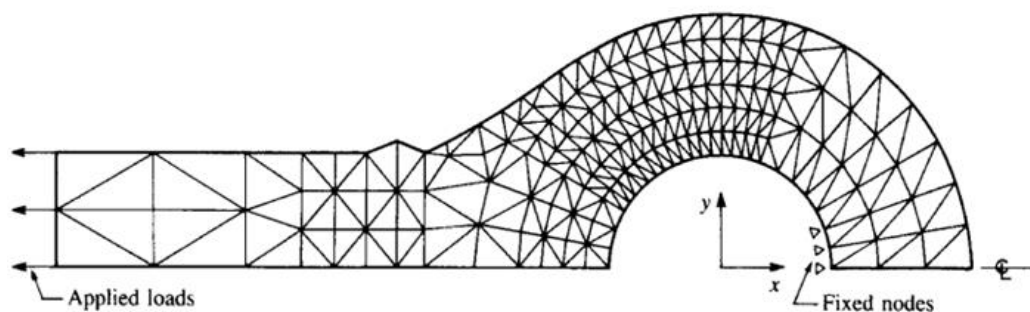
Figure 1.3 Two-dimensional analysis of a hydraulic cylinder rod end (120 nodes, 297 plane strain triangular elements) [28]

Figure 1.5 shows a three-dimensional model of the human pelvis which can be used to study stresses in the bone and the cement layer between the bone and the implant.

As previously indicated, the finite element method has been applied to numerous problems, both structural and nonstructural. This method has a number of advantages that have made it very popular. They include the ability to :

1. Model irregularly shaped bodies quite easily

2. Handle general load conditions without difficulty

3. Model bodies composed of several different materials because the element equations are evaluated individually

4. Handle unlimited numbers and kinds of boundary conditions

5. Vary the size of the elements to make it possible to use small elements where necessary

6. Alter the finite element model relatively easily and cheaply

7. Include dynamic effects

8. Handle nonlinear behavior existing with large deformations and nonlinear materials

The finite element method of structural analysis enables the designer to detect stress, vibration, and thermal problems during the design process and to evaluate design changes before the construction of
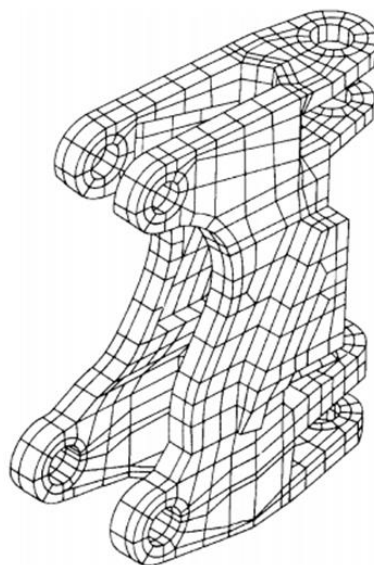
Figure 1.4 Three-dimensional solid element model of a swing casting for a backhoe frame [28]

a possible prototype. Thus confidence in the acceptability of the prototype is enhanced. Moreover, if used properly, the method can reduce the number of prototypes that need to be built. Even though the finite element method was initially used for structural analysis, it has since been adapted to many other disciplines in engineering and mathematical physics, such as fluid flow, heat transfer, electromagnetic potentials, soil mechanics, and acoustics [22--33, 27-34, 42--35]. In term of a practical structural problem, it is significant to simplify the actual model in a suitable method.

1.2 Studies in history

The use of ceramic tube for die casting has been studied by some authors [19-22]. In 2005, the using ceramic tube (stalk) for low-pressure die casting was proposed by Bonollo et al. [19]. Here, a technical and economical term of low-pressure die casting was considered. Low-pressure die casting was characterized by several advantages, including high yield, excellent control of operative parameters, good metallurgy, and technology quality. However, the ceramic tube effect in the die casting was not studied sufficiently.

Next, Noda et al. studied on the thermal stress for a ceramic stalk in the low pressure die casting machine in 2009 [20], and for ceramic stalk having protuberance dipping into molten metal in 2010 [21]. Previously, the tube was made of cast iron resulted in spoiling the quality of the product
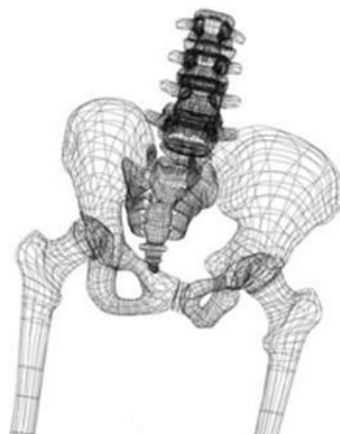
Figure 1.5 Finite element model of a human pelvis (Studio MacBeth = Science Photo Library) [28]

because of the partial melting of molten metal. Therefore, a ceramic tube was proposed to improve the lifetime. The thermal stress was investigated when the tube was dipped into the crucible by varying dipping speeds and dipping directions. It was found that for a vertical tube with or without protuberance, dipping slowly may be suitable to reduce thermal stress because dipping fast causes large temperature difference in the thickness direction, which results in large thermal stresses. However, for a horizontal tube, dipping fast may be suitable to reduce thermal stress even though it causes a larger temperature difference in the thickness direction of the tube. Moreover, since the molten metal cannot flow into the stalk with protuberance very much, the inner heat transfer coefficient μ of the stalk with protuberance is much lower than the inner μ of a simple tube.

Moreover, Ryan [22] studied how to reduce the thermal stress of the ceramic tube for low-pressure die casting. It is found that managed pre-heating is shown to best reduce stress in the riser tube, with a preheat temperature of 350C or greater predicted to protect the tube from damage during insertion in the melt and the critical initial cast. Thermal stress for all ceramics rolls used in molten metal was also investigated by Noda et al. [27]. The best way to reduce thermal stress on the ceramic roller is obtained. First, the thermal stress in the hollow cylinder can be reduced by dipping them into molten zinc fast $u = 25$mm/s. Second, for solid cylinder, the thermal stress could be reduced by dipping into molten zinc slowly. Noda et al. [35] successfully conducted research on ceramic roller used in the

(a) $\sigma_{\theta max}$ vs. δ/d and $\sigma_{\theta s}$ vs. δ/d

(b) $\sigma_{\theta b}$ vs. δ/d
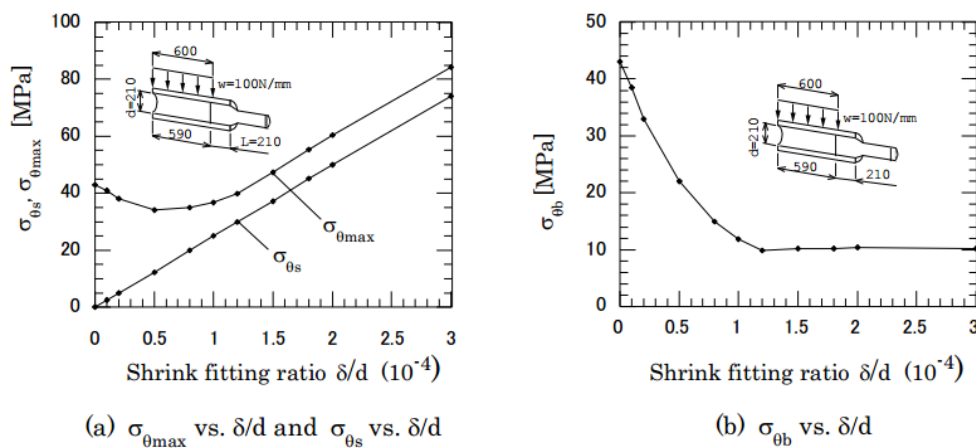
Figure 1.6 σ_{θ} vs. δ/d when $L = 210$ mm ($\sigma_{\theta max} = \sigma_{\theta s} + \sigma_{\theta c}$, $\sigma_{\theta s}$ = stress due to shrink fitting, $\sigma_{\theta s}$ = stress due to distributed load) [35]

hot rolling mills. Here, a ceramic sleeve and two short solid shafts were connected by shrink fitting whose inner diameter of sleeve d = 210mm. Ceramic roller was considered under room temperature. The results show that for large shrink fitting ratio $\delta/d = 2.0 \times 10^{-3}$, the stress due to distributed load σ_θ b becomes constant independent of δ/d as shown in Figure 1.6. The constant value coincides with the results when the sleeve and shafts are perfectly bonded. In other words, if $\delta/d \geqslant 2.0 \times 10^{-3}$, the sleeve and shaft can be treated as a unit body.

Application of large ceramic structures to steel manufacturing machinery is suitable for several steel manufacturing rolls [25, 26]. Here, a new roll structure used in the continuous pickling line was considered. Some steps have been carried out including static strength analysis as well as fatigue strength analysis for ceramic rolls. Besides stress analysis for large ceramic structures, separation conditions for shrink fitting system used for ceramic roller in hot rolling mills were also analyzed because steel shaft sometimes has to be exchanged for reconstruction [36]. It is found that the separation time becomes shorter if the atmosphere temperature went up more quickly. Generally, the separation time was influenced by several factors such as shrink fitting ratio, the outer diameter of the sleeve, the thickness of the fitted shaft and fitted length. Thermal stress was also indicated in the study by Li et al [37].

Similar ceramic structures as this new roller as is shown in Figure 1.2 under high-temperature environment in the continuous pickling line, the heating furnace, and in continuous galvanizing line have been considered in previous studies.

In recent years, Dedi et al. [41, 42] did some studies on this roller by the finite element method (see Figure 1.2). Firstly, the appropriate joint selection was considered for ceramic roller used under room temperature and high temperature. The roller consists of ceramic sleeve and steel shaft subjected to both distributed load and thermal load. Since thermal expansion mismatch between ceramic and steel is the main problem, the appropriate joint method was considered in terms of joint strength. Three types of joints were investigated as shown in Figure 1.7, namely, adhesive bonding, metal bonding, and shrink fitting. For adhesive bonding and metal bonding model, interlayer material is necessary to be considered to bond ceramic sleeve and steel shaft. Interlayer material used for adhesive bonding model is epoxy, and the one for metal bonding model is BA03/WC. For

shrink fitting, ceramic sleeve and steel shaft are connected by shrink fitting with shrink fitting ratio(interference ratio) $\delta/d = 0.2 \times 10^{-3}$. It was found that three models are quite safe under room temperature. But only shrink fitting model can be applied to ceramic roller under high temperature.

It is suggested that the shrink fitting may be the most suitable connection method for cylindrical ceramic and the maintenance cost as well as reducing replacement time of the shaft [41-43]. However, a word of caution that only a low shrink fitting ratio can be applied for those structures because of the ceramic brittleness is necessary. Meanwhile, for a slender roller structure, especially operated under elevated temperature, once both ends are fixed, it may be broken easily because of no allowance for large axial thermal deformation. Since the axial movement of the shaft cannot be constrained by the free end of the bearings for the rollers, the coming out can be problematic. And the coming out phenomenon of the shaft was observed in small prototype rollers [43].

Even when the shaft movement is constrained within a small allowable range, the coming out of the shaft may cause frictional heat generation, local thrust loading, and wear leading to uncertain operation failure of the roller [42]. Previously, Truman and Booker investigated micro-slipping between the gear hub and shaft connected by shrink fitting [38]. Antony analyzed
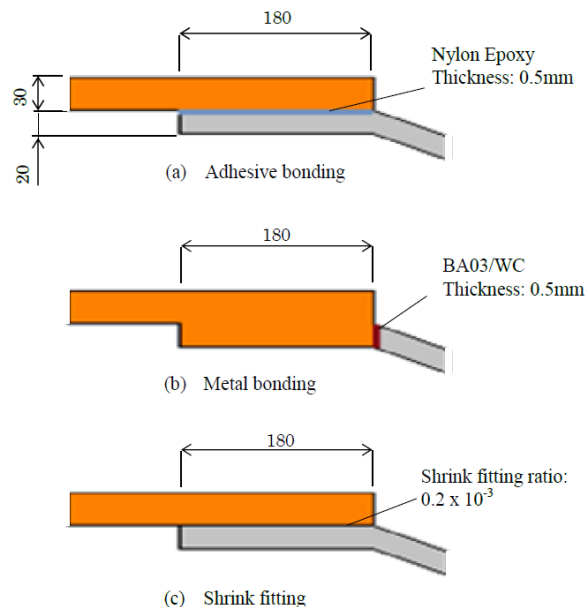
Figure 1.7 Three types of joints

contact separation for rotating thermos-elastoplastic shrink fit assembly [39]. However, few failure studies are available for coming out of the shaft from the shrink-fitted ceramic sleeve. The finite element method was applied to simulate the coming out behavior.

Dedi et al.[42] used the finite element method to realize the coming out phenomenon simulation for the roller shown in Figure 1.2 and Figure 1.8. In the first place, the inertial force effect during the roller rotation was considered by assuming a two-dimensional rotating disk as is shown in Figure 1.9. Then the shrink fitting ratio may be reduced by only 0.12% because of the roller rotation [42,44]. Since the inertial force can be neglected, a quasi-static analysis was proposed. The roller rotation is replaced by a shifted load in the circumferential direction on the fixed roller. It is found that the load rotation can be approximated by the discrete load shifting at the interval angle $\theta_0 = 12°$ within 1% error as is shown in Figure 1.10 [42]. Although the fundamental coming out failure analysis was
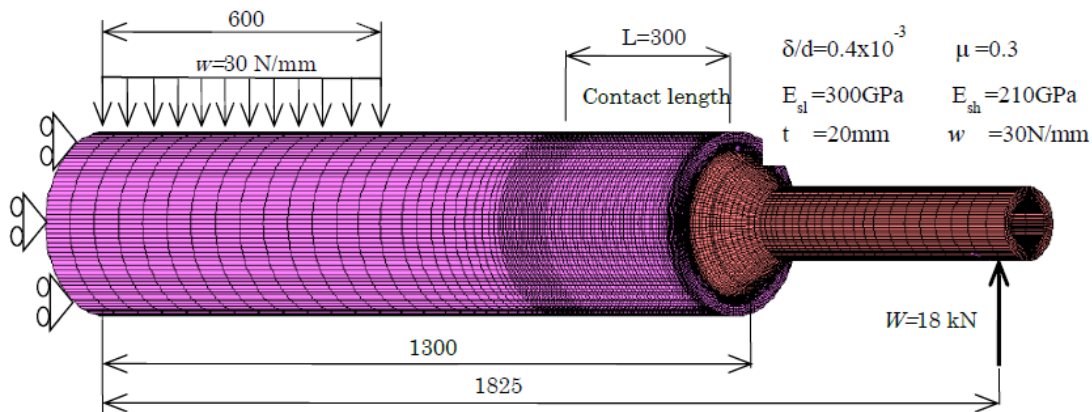
Figure 1.8 Half model with FEM mesh [42]
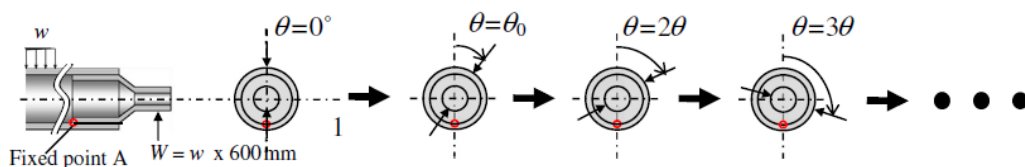
Figure 1.9 The rotation of the roller replaced by the shifted load at the interval of the load shift angle θ_0. When $\theta = 0°$ the number of cycle N=0, and when $\theta = 360°$ the number of cycle N= 1 [42]

conducted, the computation time was too large to get sufficient loading circles.

To predict the coming out behavior more accurately and to realize a large number of loading cycles, the simplified two-dimensional model was considered as is shown in Figure 1.11. Xu [43] et.al developed a two-dimensional model to reduce the calculation time and obtained the results when the number of cycle N is larger than 10. Figure 1.12 shows the results of the coming out displacements depending on the loading cycles [43].

Those studies [25~27,35~37,41~ 43] have proved that the coming out behavior can be realized by the two-dimensional and three-dimensional simulations, and the finite element method is very
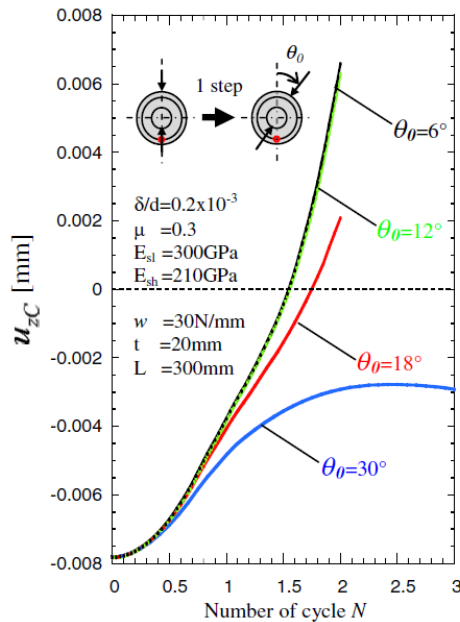
Figure 1.10 The z-displacement at center point C u_{zC} vs. number of cycle N for different θ_0 when $\delta/d = 0.2 \times 10^{-3}$ and μ=0.3 [42]
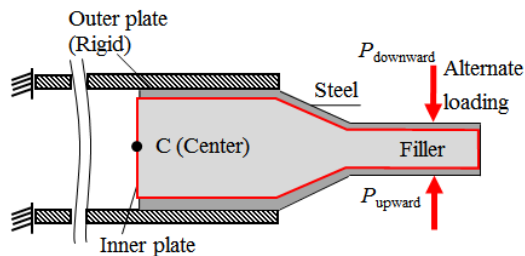
Figure 1.11 2D model in the previous paper [35]

effective and useful for failure analysis and structure design for this kind of roller. However, the driving out force F_d and its generation mechanism are not clarified. For the analysis by three-dimensional FEM model, the computational time is also enormous.

1.3 Objective and scope of the present work

The objectives of this research are:

(1) To find out the coming out mechanism (generation mechanism of the driving out force F_d) and clarify the coming out process of the shaft from the sleeve in a much more understandable way with less computational time for a large number of loading cycles.

(2) Before analyzing the actual three-dimensional real model, it is extremely useful to investigate the effects of important design factors on the driving out force generated on the shaft.

(3) To calculate the driving out force F_d^{3D} for an actual three-dimensional model, and try to design the actual structure, to investigate the effect of the shrink fitting ratio on the coming out of the shaft from the ceramic sleeve as well as some other parameters. The scope of the present work will be carried out through the following stages.
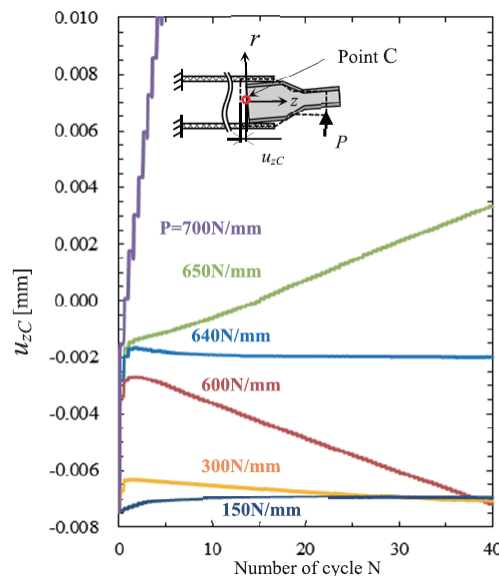
Figure 1.12 Displacement u_{zC} vs. number of cycle N for different load P when δ/d $= 0.2 \times 10^{-3}$.

The first stage is to find out the coming out mechanism of the shaft from the sleeve with less computational time, based on the previous studies, a two-dimensional simplified model with a newly installed stopper were used to conduct the coming out simulation. A two-dimensional shrink-fitted structure is considered by replacing the shaft with the inner plate and by replacing the sleeve with the outer plate. The inner shaft gradually comes out until stopped by the stopper under the standard simulation condition. This is because a kind of driving out force F_d is generated on the shaft when the alternate load is applied. Then the generation mechanism of the driving out force is clarified.

In the second stage, it is extremely useful to deeply understand the shaft coming out phenomenon and the mechanism by simulating a large number of cycles with a two-dimensional model before analyzing and designing the real roller structure. The effect of the shrink fitting ratio on the driving out force of the shaft is discussed as well as several other parameters, such as Young's modulus of the shaft, the friction coefficient, magnitude of the load, etc. Suitable conditions are discussed to design a structure to help prevent this coming out failure in the future.

In the third stage, to find out the coming out mechanism and to calculate the driving out force F_d^{3D} for an actual three-dimensional model, and try to design the actual structure. A novel Ball-stopper designed for the three-dimensional model originally to fertilize the mechanism analysis and calculation of F_d^{3D} is introduced. It is a very convenient approach. The function of this kind of Ball-stopper is firstly proved by comparing with the stopper used in the two-dimensional model. Then further simulation will be performed.

1.4 Thesis outlines

This thesis consists of five chapters. Chapter 1 provides the problem statement and motivation of the study. Also, it provides a review of the recent research on ceramic rolls. The objectives and thesis layout are also available at the end of this chapter.

In Chapter 2, to simplify the three-dimensional roller, a two-dimensional simulation was considered by adding the stopper help to clarify the mechanism of the coming out phenomenon. The contact force at the stopper is regarded as the driving out force. To explain the driving out force

generation mechanism, the equilibrated forces are considered among the frictional shear forces and the contact force. The coming out process is also explained in terms of the residual displacement.

In Chapter 3, the driving out forces F_d can be calculated as the contact force appears at the stoppers as well as the resultant frictional shear forces along with the downside and upside of the fitting portions. Then, the effects of several design factors on the driving out force are discussed. Here, the friction coefficient, shrink-fitting ratio, shrink-fitted length, and Young's modulus of the inner shaft are considered as the most fundamental design factors. For the effect of each of the factors, a unique characteristic is found. It is useful to perform the two-dimensional model simulation before the analysis of the actual three-dimensional model. When designing a three-dimensional real roller, the maximum value of the driving out force F_d should be acquired based on the behavior clarified in this study, and used for the strength design of the stopper. Thus, the knowledge obtained by this two-dimensional model analysis can be applied to the analysis of the three-dimensional model in the future for next procedure and to the design of the stopper structure that receives the driving out force F_d.

In Chapter 4, to find the mechanism by three-dimensional real model and to calculate F_d, a ball stopper is designed for accepting F_d for convenient analysis. The roller rotation is replaced by the shifted load in the circumferential direction on the fixed roller. Before applying the Ball-stopper to the three-dimensional model, a two-dimensional model is used to prove the effectiveness of the Ball-stopper. F_d and the frictional shear forces are observed to be balanced with each other, which is coincident with the two-dimensional model. As the most fundamental design factors, the effects of the shrink fitting ratios and friction coefficients on the driving out forces appeared on the shaft are also discussed.

Finally, Chapter 5 provides the major conclusions, the most significant outcomes and contributions and suggestions for future works.

1.5 Reference of chapter 1

[1]   Barsoum, M.W., Fundamentals of ceramics, Tailor&francis, Boca Raton, FL, 2003

[2]   Carter, C.B. and Norton, M.G., Ceramics materials, Springer, new York, 2007

[3]   Chiang, Y.M., Birnie, D.P., and Kingery, W.D., Physicla ceramics, John wiley&sons, New York, 1997

[4]   Richerson, D.W., Modern ceramic engineering: properties, processing, and use in design. CRC pres, Salt Lake City, UT, 1992

[5]   Davidge, R. W., Mechanical behavior of ceramics, Cambridge university press. John Wiley&Son, UK, 1979

[6]   Larsen, R. P. and Vyas, A.D., The outlook for ceramics in heat engines:1900-2010, SAE Paper No. 880514, Society of Automotive Engineers, Dearborn, MI, 1998

[7]   Wray, P., Advanced structural ceramics: Tech Monitoring, SRI International, Japan, 1991

[8]   Hori, Y., Miyakawa, Y., Asami, S., and Kajihara, T., Si3 N4 Ceramic Valves for Internal Combustion Engines, SAE Technical Paper 890175, 1986

[9]   Ogawa, Y., Machida, M., Miyamura, N., Tashiro, K. et al., Ceramic Rocker Arm Insert for Internal Combustion Engines, SAE Technical Paper 860397, 1986

[10] Ogawa, Y., Ogasawara, T., Machida, M., Tsukawaki, Y. et al., Complete

[11] Ceramic Swirl Chamber for Passenger Car Diesel Engine, SAE Technical Paper 870650, 1987 Jahanmir, S., Friction and wear of ceramics, Marcell Dekker, New York, 1994

[12] Woydt, M., and Habig, K. H., High Temperature Tribology of Ceramics, Tribol. Int. 22, pp. 75-88, 1989

[13] Matsubara, H., Miyashita, K., Iguchi, Y., Tanaka, S. et al.,   Superior Charging Technology by Screw Supercharger and High Technology Turbocharger for Automotive Use, SAE Technical Paper 890455, 1989

[14] Kawase H, Kato, K et al., Development of ceramics turbocharger rotors for high temperature use, ASME paper no 91-GT -270, 1991

[15] Kanazawa, N., Niwa, K., and Sugimoto, T., The automotive ceramic gas turbine development results in Japan, Industrial Ceramics, 19, pp. 179-183, 1999

[16] Mikami, T., T anaka, S., T agashira, K., and Koga, S., Application of ceramics to THE CGT301, A 300 kw class ceramic gas turbine, Industrial Ceramics, 19, pp. 184-188, 1999

[17] Whitney, D. E., Ceramics cutting tools: Materials, Development, and Performance, Noyes

Publication, New Jersey , USA, 1994

[18] U. Dworak, High-tech ceramics: Viewpoints and perspectives, ed. by K. Gernot, Academic Press Limited, London, 1, 1989.

[19] Bonollo, F., Urban, JR., Bonatto, B., and Botter, M., Gravity and low pressure die casting of aluminium alloys: a technical and economical benchmark, Alluminio E Leghe, 6, pp.23-32, 2005.

[20] Noda, N.A., Hendra, Takase, Y., Li, W., Thermal stress analysis for ceramics stalk in the low pressure die casting machine. Journal of Solid Mechanics and Material Engineering, 3, pp.1090-1100, 2009.

[21] Noda, N.A., Hendra, Li, W., and Takase, Y., Thermal stress and heat transfer coefficient for ceramics stalk having protuberance dipping into molten metal. Journal of Solid Mechanics and Material Engineering, 4(8), pp.1198-1213, 2010.

[22] Ryan, M.J., et al: Prestresse sialon aluminum-casting riser tubes. JACS, 49(2013), 44.

[23] Ogawa, E., et al., Proceedings of 8th International Conference on Zinc and Zinc Alloy Coated Steel Sheet, Hdg Process Technologies, (2011), 1.

[24] Miki, E., High corrosion resistance and cost reduction by spraying methods, Plant Engineer, 21(1), pp. 8, 1989.

[25] Noda, N.A., Sano, Y., Takase, Y., Li, W., and Sakai, H., Application of large ceramics structures to steel manufacturing machinery, International Journal of Engineering Innovation and Management, 1, pp.77-82, 2011.

[26] Ogawa, E., et al., Practical evaluation of large ceramics rolls for continuous hot dipping steel sheet production line, Hitachi Metals Technical Review, 28(2012), 50-54

[27] Noda, N.A., Yamada, M., Sano, Y., Sugiyama, S., and Kobayashi, S., Thermal stress for all-ceramics rolls used in molten metal to produce stable high quality galvanized steel sheet, Engineering Failure Analysis, 15, pp.261-274, 2008.

[28] A First Course in the Finite Element Method, Daryl L. Logan, 5ed, Cengage, 2012,1-29[有限元书]

[29] Hrennikoff, A., ''Solution of Problems in Elasticity by the Frame Work Method,'' Journal of Applied Mechanics, Vol. 8, No. 4, pp. 169–175, Dec. 1941.

[30] McHenry, D., ''A Lattice Analogy for the Solution of Plane Stress Problems,'' Journal of Institution of Civil Engineers, Vol. 21, pp. 59–82, Dec. 1943.

[31] Turner, M. J., Clough, R. W., Martin, H. C., and Topp, L. J., ''Stiffness and Deflection Analysis of Complex Structures,'' Journal of Aeronautical Sciences, Vol. 23, No. 9, pp. 805–824, Sept. 1956.

[32] Zienkiewicz, O. C., and Cheung, Y. K., ''Finite Elements in the Solution of Field Problems,'' The Engineer, pp. 507–510, Sept. 24, 1965.

[33] Lyness, J. F., Owen, D. R. J., and Zienkiewicz, O. C., ''Three-Dimensional Magnetic Field Determination Using a Scalar Potential. A Finite Element Solution,'' Transactions on Magnetics, Institute of Electrical and Electronics Engineers, pp. 1649–1656, 1977.

[34] Girijavallabham, C. V., and Reese, L. C., ''Finite-Element Method for Problems in Soil Mechanics,'' Journal of the Structural Division, American Society of Civil Engineers, No. Sm2, pp. 473–497, Mar. 1968.

[35] Noda, N. A., Hendra, Takase, Y ., and Tsuyunaru, M., Maximum stress for shrink fitting system used for ceramics conveying rollers, Journal of Solid Mechanics and Materials Engineering, 2(8), pp.1410-1419, 2008.

[36] Li, W., Noda, N. A., Sakai, H., and Takase, Y., Analysis of Separation Conditions for Shrink Fitting System Used for Ceramics Conveying Rollers, Journal of Solid Mechanics and Materials Engineering; 5(1), pp.14-24, 2011.

[37] Li, W., Noda, N. A., Sakai, H., and Takase, Y., Thermal Stress Analysis for Shrink fitting System used for Ceramics Conveying Rollers in the Process of Separation, Key Engineering Materials, 452-453, pp.241-244, 2011.

[38] Truman C. E., Booker J. D., Analysis of a Shrink-fit Failure on a Gear Hub/Shaft Assembly, Engineering Failure Analysis, 14, pp. 557-572, 2007.

[39] Antoni N, Contact Separation and Failure Analysis of a Rotating Thermo-elastoplastic Shrink-fit Assembly, Applied Mathematical Modelling, 37, pp.2352-2363, 2003.

[40] Hagen, K., Silicon nitride for high temperature applications, Journal of the American Ceramics Society, 93(6), pp.1501-1522, 2010.

[41] Noda, N.A., Suryadi, D. et al.: Proposal for New Hearth Roller Consisting of Ceramic Sleeve and Steel Shafts Used in the Heat Treat Furnace, ISIJ Int., Vol. 55 (2015), No. 11, pp. 2416–2425

[42] Noda, N.A., Suryadi, D., Kumasaki, S., Sano, Y., Takase, Y.,:Failure analysis for coming out of shaft from shink-fitted ceramic sleeve, Engi. Fail. Anal.,57(2015),219.

[43] Noda, N.A., Xu, Y., Sano,Y., Takase, Y.,:Coming out mechanism of steel shaft from ceramic sleeve, ISIJ Int., 56, 2(2016), 303.

[44] S.P. Timoshenko, J.N. Goodier, Theory of Elasticity, McGraw-Hill Kogakusha Ltd., Tokyo, 1970. 81 – 82.

Chapter 2 Generation mechanism of the driving out force of the shaft from the shrink-fitted ceramic roll by introducing newly designed stopper

2.1 Introduction

Steel conveying rollers are used in the heating furnace as shown in Figure 2.1(a) for producing high-quality steel plates. The conventional common roller uses the steel material with ceramic spray coating on the outside of the sleeve. Inside of the roller is cooled by water for reducing the temperature. Since the linear expansion coefficient of steel is about 4 times larger than that of ceramics, the thermal expansion mismatch may exceed the strength of the ceramic layer and may cause failure on the roller surface such as wearing, peeling and crack[1]. Therefore, it is difficult to maintain a long life for such rollers.

Figure 2.1(c) illustrates a new ceramic roller consisting of the steel shaft connected at both ends and the ceramic sleeve having high heat resistance, high wear resistance and high corrosion resistance [2,3]. Previous studies indicated that the shrink fitting system may be the most suitable joining method for ceramic cylindrical structures to reduce maintenance time and cost for shaft replacement [4-8]. However, since most of the ceramics are quite brittle, only a small
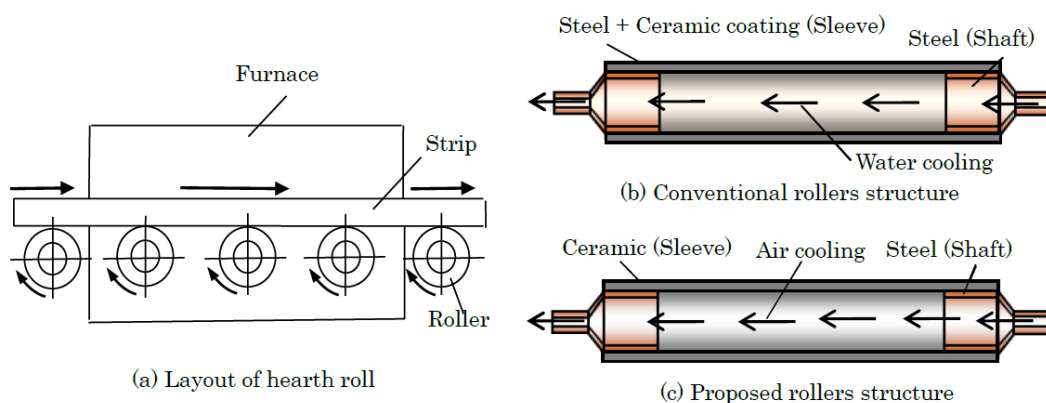
Figure 2.1 Conventional and proposed rollers for heating furnace

shrink fitting ratio can be used [9-16]. During operation, the coming out of the shaft may happen, and therefore, we have to prepare for this new failure.

In our previous studies, coming out simulations were performed for the shaft from the shrink-fitted ceramic sleeve by using the finite element method[4,5]. In Ref.[4], a three-dimensional roller model was considered by replacing the roller rotation as the load shifting on the fixed roller. Since the calculation time was very large, only the rotation cycles until $N = 5$ were conducted. Then, effects of shrink fitting ratio, friction coefficient et al. on the coming out behavior were studied. Furthermore, in Ref.[5], the two-dimensional simulation was conducted to reduce the calculation time and more than $N = 40$ cycles were investigated. Those studies [4, 5] have proved that the coming out behavior can be numerically realized on the two-dimensional and three-dimensional simulations.

As a further development of those previous studies, this study will focus on a stopper newly installed on the sleeve to evaluate the driving out force generated on the shaft. In the first place, a two-dimensional model used in Ref.[5] will be improved to prevent the coming out. To design the stopper, the contact force between the stopper and the inner plate and the resultant frictional shear forces along with the both sides of the fitting parts will be investigated. Note that this contact force can be regarded as the driving out force generated on the shaft. The discussion shown in this chapter is therefore useful for understanding the coming out mechanism.

2.2 Analysis method

In this research, in the first place, the coming out behavior will be simulated by using the elastic finite element method analysis. Next, after confirming the contact between the inner plate and the stopper, the driving out force of the coming out will be studied from the contact force.

The two-dimensional analytical model used in the previous paper [5] is shown in Figure 1.7. To simulate the behavior in a large number of cycles, the shaft is replaced by the inner plate and the sleeve is modeled as the outer plate as shown in Figure 1.7. The coming out behavior is analyzed by paying attention to the displacement at Point C.

Figure 2.2 (a) illustrates the new 2D model having the stopper whose height = 1.6 mm. The detail of

the stopper part is shown in Figure 2.2 (b). Consider Point D in Figure 2.2 (b) as the reference point for the coming out displacement of the inner plate. To simplify the analysis, the outer plate is assumed as a rigid body. The inner plate combines the steel and filler together by considering equivalent elastic modulus. This is because the hollow structure cannot be used in the 2D simulation [5,17]. Table 2.1 shows the material properties of the model. The outer plate and the inner plate are connected by shrink fitting. The shrink fitting ratio is defined as the shrink fitting value δ divided by the thickness d of the outer plate fitting portion (d = 240 mm). The shrink fitting ratio δ/d ranges from 0 to 1.0×10^{-3}. Here, in order to elucidate the basic generation mechanism of the driving out force, the shrink fitting ratio $\delta/d = 0.2 \times 10^{-3}$, the friction coefficient $\mu = 0.3$, the stopper height H = 1.6 mm are used as reference values. The boundary conditions are the same as described in the previous paper [5].

In this study, since the inertial force can be neglected [4], a quasi-static elastic structure analysis

(a) 2D model with stopper (mm)

(b) Detail of stopper (S) (mm)

(c) Alternate loading
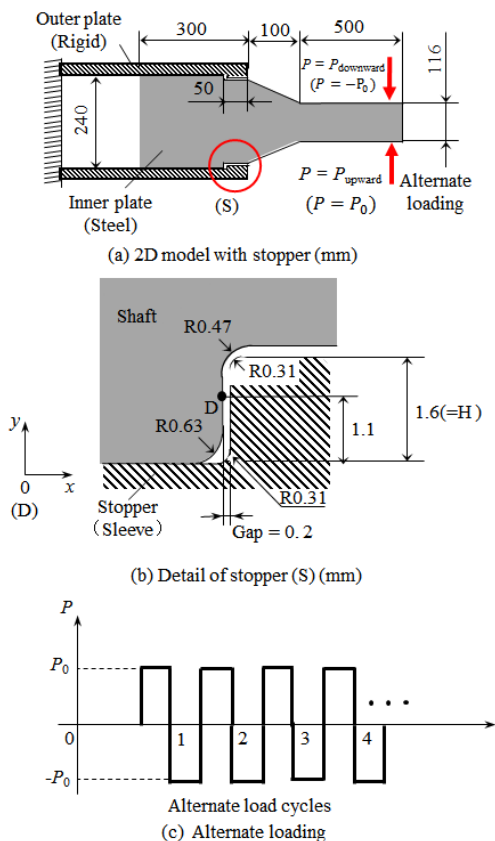
Figure 2.2. New simplified 2D model with stopper and the loading method
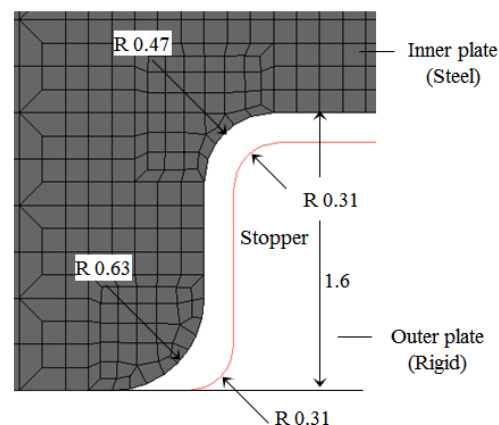
Figure 2.3 Mesh detail of the inner plate around stopper (see Figure 2.2 (b)) (Unit:mm)

is performed by using MSC Marc/Mentat 2012 with full Newton-Rapson iterative sparse solver of multifrontal method [18]. Considering the symmetry of the model, alternate loads are applied in the vertical direction to the 1/2 model as shown in Figure. 2.2(a). Here, the quadrangular contact element has been used and the number of element is 24546. In contact analysis by MSC Marc/Mentat 2012, it has been told that the Coulomb friction model can be widely used for most practical applications except for bulk forming as encountered in e.g. forging processes. Three types of Coulomb friction models are aviliable[19], that is, arctangent model, stick-slip model and bilinear model. However, it is known that the arctangent model is unsuitable for estimating the typical relative sliding velocity priori when the sliding velocity varies largely during the analysis. Also, the stick-slip model needs a large amount of data to be determined from repetitive calculation process[19]. In this study, therefore, the bilinear model is applied since the friction force is simply determined from the displacement. Figure 2.3 shows the mesh detail around the stopper and the minimum element size is 0.15625×0.15625 mm.

2.3 Conditions and mechanism for the driving out force generation

2.3.1 Generation conditions of the driving out force

When alternate load P is repeatedly applied to the inner plate in N cycles, a kind of driving out force may be generated on the inner plate. Then, the inner plate comes out gradually. However, in this study, since the stopper is installed on the outer plate, the movement of the inner plate in the axial direction can be stopped by the stopper. Here, Point D at 1.1 mm distance from the fitting surface is used to represent the contact point, the number N_c denotes the cycle when the contacting

Table 2.1 Material properties of the two-dimentional model

	Outer plate	Inner plate	
Material	Rigid*	Steel	Filler*
Young's modulus [GPa]	∞	210	52
Poisson's ratio	—	0.3	0.3
Tensile strength [MPa]	—	600	—
Mass density [kg/m³]	—	7800	7800

*Assumed in the simulation.

starts. To describe the contact condition at the stopper, the coming out of the inner plate is represented by the displacement u_{xD} in the x direction.

Figure 2.4 shows displacement u_{xD} in different loading cycles under alternate loading P. Here, the reference values, $\delta/d = 0.2 \times 10^{-3}$ and $\mu=0.3$ are used. In Figure. 2.4, before loading $N < 1$, a small displacement $u_{xD} = 0.000537$ mm caused by shrink fitting is ignored and $u_{xD} = 0$ mm is assumed before shrink fitting. When the load becomes large, the displacement u_{xD} increases with increasing N, then becomes stable after the inner plate contacts with the stopper. For example, when $P = 1000$ N/mm, the displacement reaches a constant value of 0.176 mm during the second cycle and does not change anymore. This is because $u_{xD} = 0.176$ mm means that the point D contacts with the stopper. With decreasing P, the contact starting cycle N_c increases, and when P is small enough, no contact occurs. Therefore, there is a threshold value P for the coming out. From Fig. 6, the threshold value of P is between 150 N/mm and 300 N/mm. When the load P is below this threshold, the displacement u_{xD} does not increase and the inner plate does not contact with the stopper. When the load P is above the threshold, the displacement u_{xD} increases with increasing cycles N. In Figure.2.4,
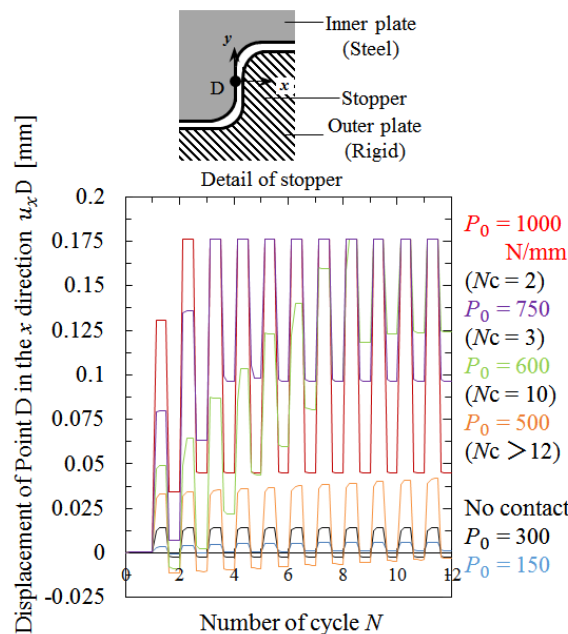
Figure 2.4 Displacement u_{xD} vs number of cycle N under different loads , fixed shrink fitting ratio $\delta/d = 0.2 \times 10^{-3}$ and friction coefficient $\mu = 0.3$

the driving out force appears if $P > 300$ N/mm for the reference condition $\delta/d = 0.2 \times 10^{-3}$ and $\mu = 0.3$.

Note that the contact force occurs at $u_{xD} = 0.176$ mm smaller than the gap amount 0.2 mm. The reason can be explained in the following way. To handle the contact problem, the amount of the contact judgement should be larger than the single side fitting amount $\delta/2$ for Msc.Marc/Mentat 2012[19]. In this study, since $\delta/d = 0.2 \times 10^{-3}$ and $d = 240$ mm, we have $\delta = 0.2 \times 10^{-3} \times 240 = 0.048$ mm. Therefore, the single side fitting amount $\delta/2 = 0.048 \times 1/2 = 0.024$ mm. Since $u_{xD} = 0.176$ mm is 0.024 mm smaller than the gap 0.2 mm, in Figure. 6, the displacement $u_{xD} = 0.176$ mm should be regarded as the contact distance between the inner plate and the stopper [20].

2.3·2 Generation mechanism of the driving out force

In this simulation, the inner plate is prevented from coming out by the stopper. Then the contact force F_s can be regarded as the driving out force. Figure 2.5 shows the relationship between the load P and the contact force F_s by changing the friction coefficient μ. Here, the cycle $N = 100$ is the maximum cycle number. When the largest friction coefficient $\mu = 0.5$, it can be seen that there is no coming out when $P \leq 750$ N/mm. As shown in Fig. 7(a), when $P \geq 875$ N/mm the contact force F_s
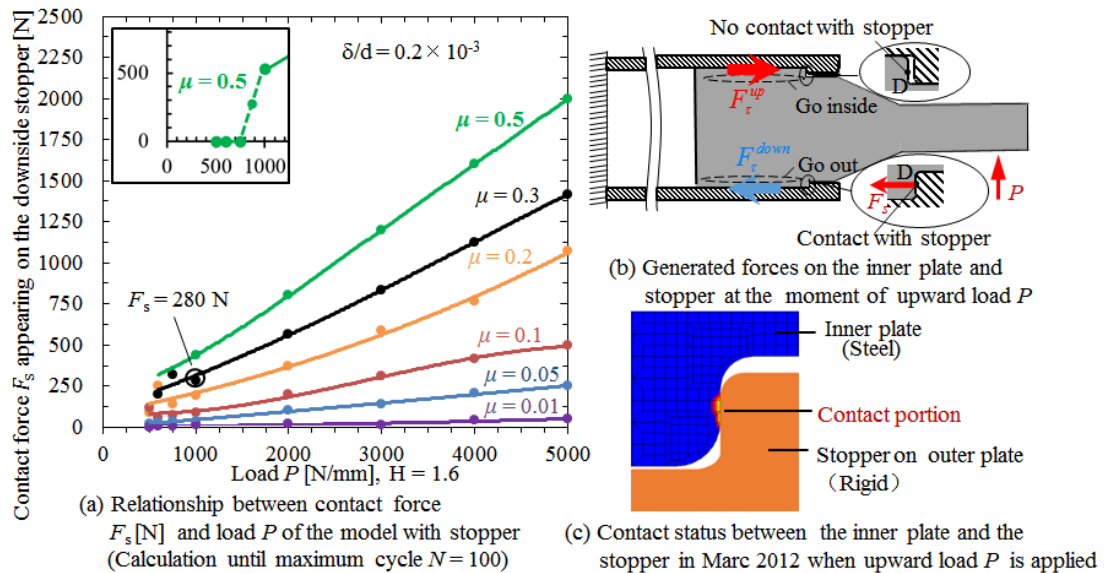
Figure 2.5. Relationship between load P and contact force F_x under different friction coefficient μ when the upward load P is applied and $\delta/d = 0.2 \times 10^{-3}$

increases with increasing load P. When $\mu = 0.3$, F_s increases almost proportionally with increasing load P when $P \geq 600$ N/mm.

In Figure. 2.5, with decreasing the friction coefficient μ, the contact force F_s decreases. When there is no friction as $\mu = 0$, F_s does not appear. In this way, it is seen that the contact force F_s is controlled by the friction coefficient μ of the fitting surface.

When the inner plate is subjected to the alternate loading P, the frictional shearing force generated on the fitting surface is balanced with the contact force F_s at the stopper. In Figure 2.5(b), from the shearing force $F_{\tau u}$ on the upside surface and the shearing force $F_{\tau d}$ on the downside surface, the contact force F_s can be expressed as the following equation.

$$F_s = F_\tau^{up} + F_\tau^{down} \tag{1}$$

For example, in Figure 2.5(a), under $P = 1000$ N/mm and $\mu = 0.3$, when the inner plate contacts with the stopper, we have $F_\tau^{up} = 1272$ N, $F_\tau^{down} = -992$ N. By substituting into equation (1) we have a contact force $F_s = 280$ N, which can be regarded as the driving out force.

2.4 Discussion on the coming out process

2.4.1 Relationship between the displacement of the inner plate and the contact force

In the previous section, the effect of the magnitude P and the friction coefficient μ on the coming out has been considered by focusing on the displacement u_{xD} at Point D. This section considers how the displacement u_{xD} and the contact force F_s appear and increase under the alternate loading.

Figure 2.6 shows the displacement at Point D and the contact force appearing at the downside stopper under the loads in Figure 2.6(a-1) and Figure 2.6(b-1). Here, the reference values $P = 1000$ N/mm, $\mu = 0.3$, $\delta/d = 0.2 \times 10^{-3}$ are used in the simulation. Under the loading in Figure 2.6 (a-1), the displacement is shown in Figure 2.6(a-2) and the contact force is shown in Figure 2.6(a-3). In contrast to Figure 2.6(a-1), as shown in Figure 2.6(b-1), the no-load interval is newly added between alternate loading. This is to clarify the coming out process by considering the displacement under no loading period. Figure 2.6(a-2) shows the displacement u_{xD} corresponding to the load pattern of Figure 2.6(a-1). The upward load (step I) and the subsequent downward load (step III) compose the first cycle. Figure 2.6(b) shows that the load (b-1) causes the displacement (b-2) different from the

one in Figure 2.6(a -2). As shown in Figure 2.6(b-2), in the second cycle where the contact force becomes stable, it is seen that the displacement of step II_2 under the downward load is larger than the step IV_2 under the upward load. New displacement steps II_2, IV_2 appear during the no-load interval. Depending on the direction of the applied load, different displacements occur irreversibly even under the no-load step. This irreversible behavior may cause the coming out behavior. The remaining displacement under no-load step is called 'residual displacement' in this study.

2.4.2 Coming out process explained in terms of the residual displacement

This section focuses on the entire fitting area of the inner plate including point D. Then, the residual displacement will be considered to explain the coming out. Figure 2.7 shows the coming out process under the loading in Figure 2.6(b-1). Figure 2.7(a) shows the equilibrium between the frictional shearing force generated and the contact force at the stopper. Figure 2.7(b) shows the deformation and the displacement over the entire fitting portion. The dotted line shows the entire fitting portion shape after shrink fitting and before alternate loading. The solid line shows the deformation and the displacement under loading. In Figure 2.7(b), the deformation is enlarged in the x-direction for the reader's convenience.

When the first upward load (step I_2 in Figure 2.6(b-2) and Figure 2.7(b-2)) is applied, Point D moves in the coming out direction, but does not contact with the stopper. Then, the shear forces on the upside and downside surfaces of the inner plate are balanced. In the no-load interval (step II_2), Point D goes back to the inward direction but does not return completely. Therefore, Point D is in the residual displacement state. Here, the shearing forces change the directions but still maintain the balance. Next, in step III_2 where a downward load is applied, Point D' on the upper surface comes into contact with the stopper while slight displacement of Point D in the coming out direction has been left. The contact force of upside stopper is 114 N which does not reach the full contact force 280 N appearing at the second cycle of step I_2. In this step III_2, the residual displacements are generated in both of the upside and downside, and therefore, the coming out process has been analytically demonstrated. At the end of the first cycle (step IV_2, no load), both of the residual displacements of Point D and Point D' keep on moving in the coming out direction, and the coming out behavior of the entire inner plate becomes significant. Although the residual displacement of

Point D at the end of the second cycle increases, it becomes stable in the subsequent cycle as shown in Figure 2.6(b-2). Next, the reason why the residual displacement occurs will be explained during the coming out simulation.

Figure 2.8 compares the deformation and the displacement over the entire fitting portion (a) under the upward loading and (b) after removing the upward loading. Here, the fitting pressure σ_f always exists along the fitting portion. When the upward load is applied, shearing forces F_τ^{up}, F_τ^{down} occur along the fitting surface so as to maintain the balance with the moment caused by the loading. Therefore, the fitting portion is deformed into a diamond shape, Point D moves in the coming out
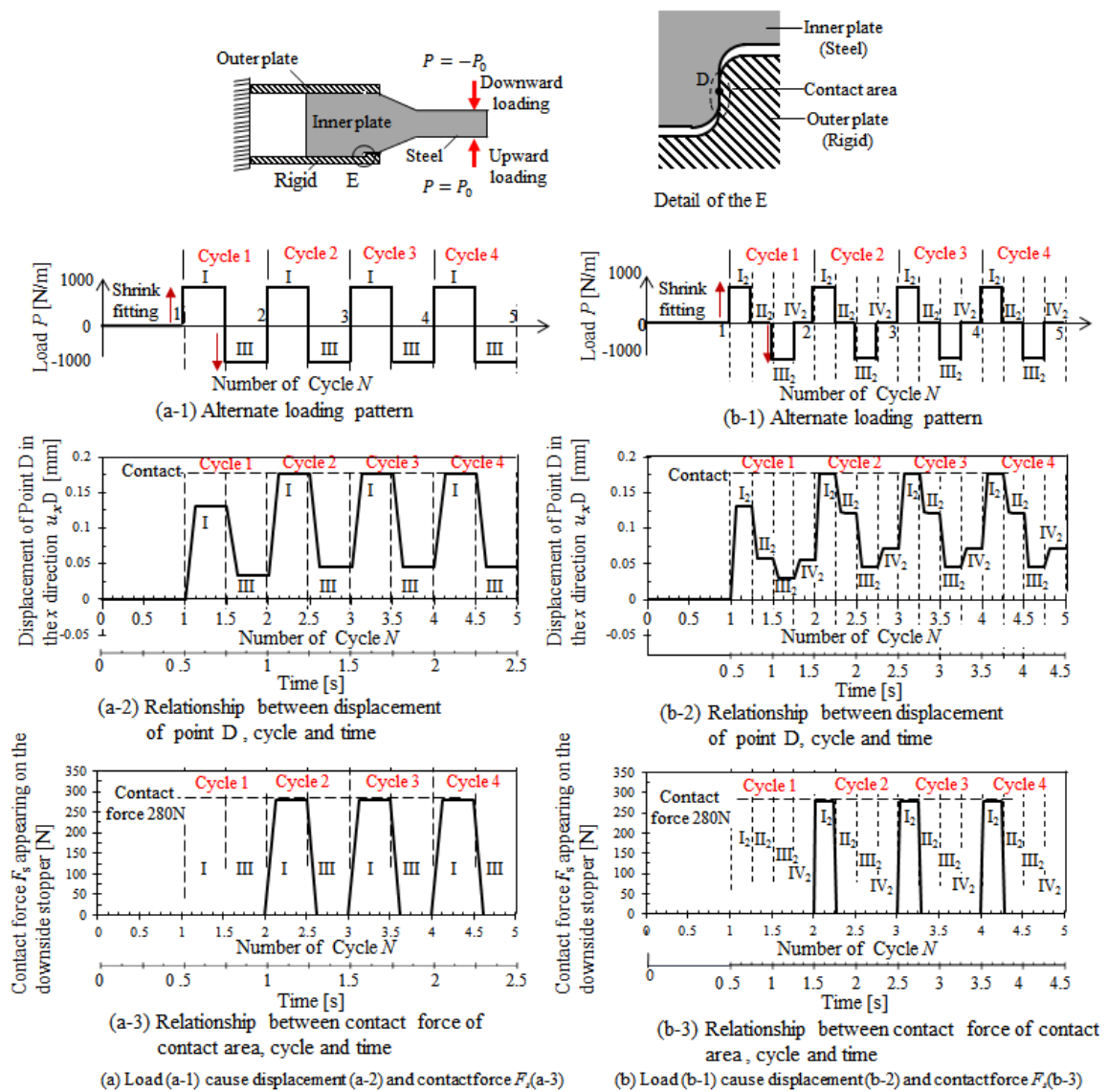
Figure 2.6 Displacement of Point D and contact force F_s when load P = 1000 N/mm, μ =0.3, $\delta/d = 0.2 \times 10^{-3}$

direction, and Point D' moves in the opposite direction. When the bending load P is removed, since
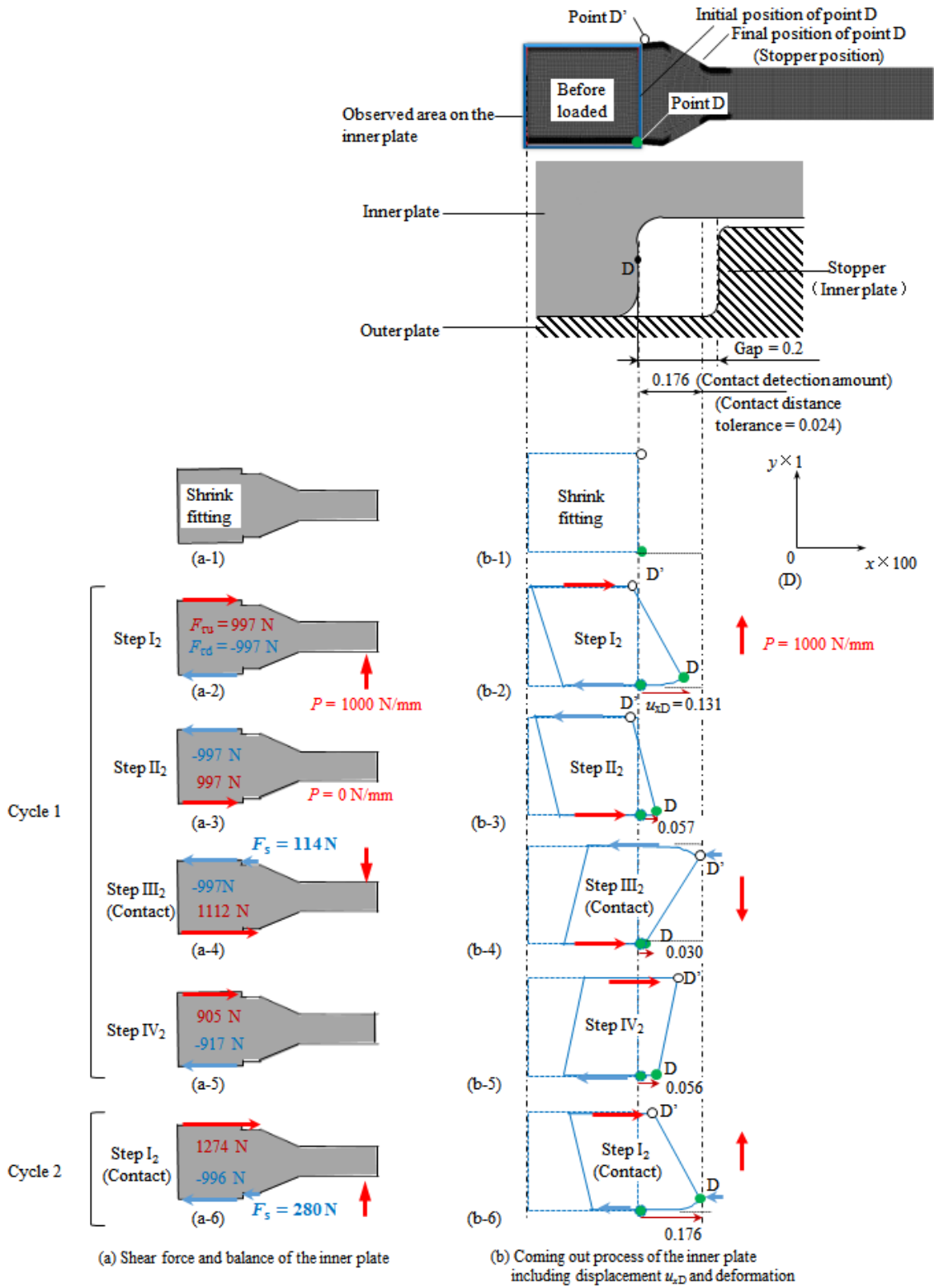
Figure 2.7 The coming out process of the inner plate when the load is 1000 N/mm in the 1st, 2nd cycle (mm)

the moment due to the external force disappears, the diamond shape of the fitting portion tries to return to the original shape. Then, the deformation around Point D decreases, but the deformation is restricted by the reverse shearing force caused by the fitting pressure and friction. Therefore, Point D does not return to the original shape completely and the residual displacement remains. Accumulation of this residual displacement causes the inner plate coming out. It can be seen that the presence of fitting pressure and the friction dominate the deformation, which results in the residual displacement. In this way, the shaft coming out process can be explained in terms of the residual displacement.

2.4.3 Application to the shrink-fitting roller

In previous studies[4], without stopper (see Figure 2.1(c)), the three-dimensional coming out simulation was carried out by replacing the rotation under bending load as the load shift on the fixed roller. Subsequently, a two-dimensional simulation was conducted under an alternate loading [5]. Then, the coming out phenomenon was realized by using the two-dimensional simulation, which can be applied to the three-dimensional shape. In this study, a new model with stoppers was considered in two-dimensional simulation similarly to the previous studies. The coming out process has been
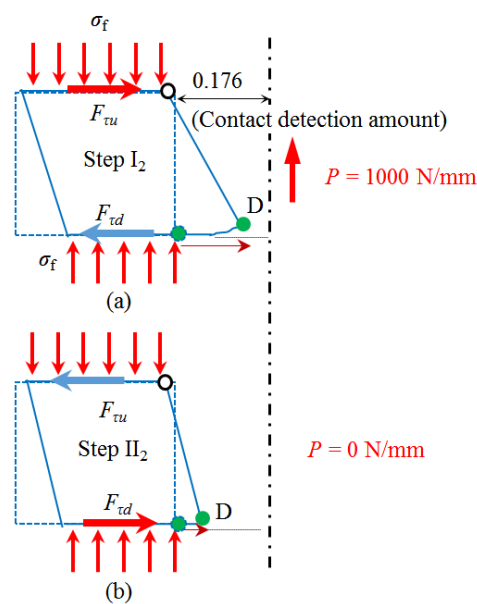
Figure 2.8 Schematic diagram of the mechanism of residual displacement of the inner plate (Unit: mm)

clarified in this study, and this approach can also be applied to the actual three-dimensional roller to prevent coming out of the shaft from the ceramic sleeve.

2.5 Conclusions

In this chapter, by developing our previous studies, the driving out force is discussed to design the ceramic rolls. To simplify the three-dimensional roller, two-dimensional simulation is considered by adding the stopper to help to clarify the coming out mechanism. The contact force at the stopper can be regarded as the driving out force F_d. To explain the driving out force generation mechanism, the equilibrated forces are considered among the frictional shear forces and the contact force. The coming out process is also explained in terms of the residual displacement. The conclusions can be summarized in the following way.

(1) Shear forces are generated along the upside and downside at the fitting portions of the inner plate to balance the alternate bending load. The inner plate comes out gradually when the shear forces in the coming out direction exceeds the shear force in the opposite direction.

(2) When the alternate loading is applied under the condition of (1), the inner plate and the stopper come into contact with each other. The contact force generated on the stopper can be regarded as the driving out force.

(3) In order to clarify the coming out phenomenon and generation mechanism, no-load interval was introduced into the alternate bending loading cycle. As a result, it was found that the residual displacement appears during the no-loading interval. The coming out process can be explained in an easy understand way by the accumulation of this residual displacement.

(4) The driving out force can be generated by the shrink fitting force, the friction force, and the bending load as shown in Figure 2.8.

2.6 References of chapter 2

[1]   M. Fujii, A. Yoshida, J. Ishimaru, S. Shigemura, K. Tani: *Trans. Jpn. Soc. Mech. Eng. C*, **72**(2006), 1354.

[2]   C.R. Liou, T. Mori, H. Kobayashi, T. Mitamura: *JCS-Jpn*, **98** (1990), 348.

[3] T. Ono: *J. Jpn. Soc. Mech. Eng.*, **86**(1983), 470.

[4] N.A. Noda, D. Suryadi, S. Kumasaki, Y. Sano, Y. Takase:*Engi. Fail. Anal.*,**57**(2015)219-235.

[5] N.A. Noda, Y. Xu, Y. Sano, Y. Takase: *ISIJ Int.*, **56**(2016), No. 2, pp. 303–310.

[6] W. Li, N.A. Noda, H. Sakai, Y. Takase: *J. Solid Mech. Mater.Eng.*, **5**(2011), 14.

[7] W. Li, N.A. Noda, H. Sakai, Y. Takase: *Key Eng. Mater.*, **452-453** (2011), 241.

[8] A. Rusin, G. Nowak, and W. Piecha: *Engi. Fail. Anal.*, **34**(2013), 217.

[9] E. Ogawa, K. Shimizu, S. Hamayoshi, N. Kumagai, Y. Ohtsubo, N.A. Noda, Y. Takase, K, Kishi, K. Shobu, T. Tabaru, E, Maeda, S. Koga, T. Matsuda: *Hitachi Metals Tech.Rev.*, **28**(2012), 50.

[10] M. Tsuyunaru, N.A. Noda, Hendra, Y. Takase: *Trans. Jpn. Soc. Mech. Eng. A*, **74**(2008), 919.

[11] N.A. Noda, Hendra. Y. Takase, M. Tsuyunaru: *J. Solid Mech. Mater.Eng.*, **2**(2008), No.11, 1410.

[12] N.A. Noda, M. Yamada, Y. Sano, S. Sugiyama, S. Kobayashi: *Engi. Fail. Anal.*, **15**(2008), 261.

[13] N.A. Noda, Hendra, M. Oosato, K. Suzumoto, Y. Takase, W. Li : *Key Eng. Mater.*, **462** (2011), 1140.

[14] S. Matsuda, D. Suryadi, N.A. Noda, Y. Sano, Y. Takase, S. Harada : *Trans. Jpn. Soc. Mech. Eng. A*, **79**(2013), 989.

[15] N.A. Noda, D. Suryadi, S. Matsuda, Y. Sano, Y. Takase: *ISIJ Int.*, **55**(2015), 2416.

[16] S.Harada, N.A.Noda, O.Uehara and M.Nagano: *Trans. Jpn. Soc. Mech. Eng. A*, **57**(1991), 539, 1637.

[17] N.A.Noda, Y.Sano, Y.Takase, S.Harada, D.Suryadi and S. Kumasaki: *Tetsu-to-Hagané*, **101**(2015), 284,(in Japanese).

[18] Marc Mentat team: Theory and User Information, Vol.A, MSC.Software, Tokyo, (2012),713.

[19] Marc Mentat team: Theory and User Information, Vol.A, MSC.Software, Tokyo, (2012),545.

[20] Marc Mentat team: Theory and User Information, Vol.A, MSC.Software, Tokyo, (2012),572.

Chapter 3 Effects of design factors on the driving out force generated on the steel shaft in a shrink-fitted ceramic roller

3.1 Introduction

Figure 1.2 shows an example of a ceramic sleeve roller developed recently, which can be widely used in heating furnaces (see Figure 1.1, 2.1(a)) of steel manufacturing industries efficiently [1-6]. Ceramics are widely used because they have high corrosion resistance [7], heat resistance and wear resistance [8]. Previous studies indicated that the shrink fitting system might be the most suitable connecting method for ceramic cylindrical structures with steel shafts to reduce maintenance time and cost for shaft replacement [9-11]. However, since only small shrink fitting ratios can be applied due to the ceramics' brittleness and the free end of the bearing for the roller do not restrict the axial movement of the shaft [12-23], the coming out of the shaft from the sleeve appeared during operation [20-22]. To solve this problem, the authors have performed a series of numerical simulation studies after the validity of the finite element method simulation was verified by an experimental test of an Ono type rotary bending fatigue-testing machine [20-22,24].

In the first place, the coming out simulation was realized in a three-dimensional model in Figure 1.2 [20]. The shaft gradually comes out under the standard simulation condition [20]. This is because driving out force F_d is generated on the shaft when the cyclic load is applied. Previously, the coming out simulation was realized by using a three-dimensional model where the roller rotation is replaced by load shifting with enormous calculation time (see Figure 1.2) [20,21]. However, the calculation time was considerable, and it was challenging difficult to analyze the coming out mechanism, not to mention the calculation of F_d [20,21]. Therefore, to realize the coming out phenomenon simulation by much more number of cycles which are necessary for analyzing of the coming out mechanism with less time, a two-dimensional model in Figure 1.7 was considered [21]. Furthermore, based on the two-dimensional model in Figure 1.7, a model with stopper was proposed to clarify the generation mechanism of the driving out force F_d of the shaft and to calculate F_d as is shown in Figure 3.1.

In the absence of the stopper, the coming out displacement of the inner plate (corresponding to the

shaft of the three-dimensional model) gradually increases until the inner plate comes off the outer plate (corresponding to the sleeve of the three-dimensional model). However, by providing the stopper, the inner plate comes into contact with the stopper while it comes out and the contact force F_s is generated. This contact force can be regarded as driving out force F_d causing the coming out of the inner shaft. Then, the generation mechanism of the driving out force was clarified by the details of displacements, deformation, and balanced forces during the coming out process. Similarly, because the simulation of the three-dimensional model with a similar stopper installed on the tail edge of the sleeve takes much more time and the contact position between the stopper and the shaft is irregularly changed by the rotation of the roll, this new two-dimensional model with stopper (see Figure) will be used to investigate the effect of some important design factors on the driving out force F_d .

In this study, therefore, by extending those previous studies, the effects of friction coefficient μ, fitting ratio δ/d, fitting length l and Young's modulus E on the driving out force F_d will be investigated by two-dimensional simulations by a large number of loading cycles. It is an indispensable and useful study prior to the analysis of the real three-dimensional model of Figure 1.2. To clarify the effect of the design factors on F_d will also help us understand the coming out phenomenon and the coming out mechanism deeply.
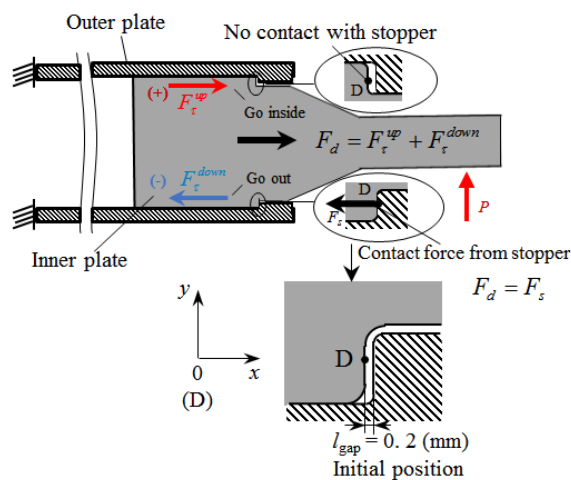
Figure 3.1 .Generation mechanism of the driving out force F_d balanced with the reaction F_s at the stopper.

3.2. Analysis Method

The FEM is one of the most used numerical modeling techniques, which can be used for many engineering applications conveniently [25-30]. Here, the coming out simulation was numerically realized by using this two-dimensional model (see Figure 3.1) under the alternate loading within much less calculation time compared to the three-dimensional model. For the currently used computer (CPU: 8 core, Frequency: 3.7 GHz, Memory RAM: 32G), it takes about a week to simulate five cycles by three-dimensional model. However, using the two-dimensional model in Figure 3.1, it can simulate 40 cycles or more in a period of about 1/15. That is, it can be said that the shortening effect is $1/15 \times 5/40 = 1/120$. The inner plate comes out gradually under the alternate loading, goes across the gap set between the inner plate and the stopper and finally contacts with the stopper. The reaction force appears at the stopper can be regarded as the driving out force correctly. As shown in Figure 3.1, frictional shear forces F_τ^{up} and F_τ^{down} appear along the upside and downside fitting portions. Then, the driving out force F_d can be expressed as the sum of those frictional forces, that is, $F_d = F_\tau^{up} + F_\tau^{down}$ Figure 4 illustrates how to generate the driving out force. In Figure 4, the driving out force F_d is balanced with the contact force F_s ($F_s = F_d$) while the inner plate comes into contact with the downside stopper.

The details of the dimensions and loading pattern used in this chapter is shown the same as Figure 2.2, 2.3. Due to the symmetry, a half model was used. Figure 2.3 illustrates the detail dimensions of the stopper. In Figure 2.3, the geometry is designed carefully so that the inner plate does not interfere with the stopper even when the load P becomes ten times larger than the reference load $P = 1000N/mm$. Also, to save the calculation time, the gap shown in Figure 3.1 should be set as small as possible, here it is set to be $l_{gap} = 0.2$ mm. Also use the material properties of the model as shown in Table 2.1. To simplify the simulation and save computational time for this model, the outer plate is assumed as a rigid body because the ceramic sleeve is generally much more rigid than the steel shaft. This is a reasonable assumption since the focus in this work is to investigate the effect of design factors on the driving out force by two-dimensional model prior to actual three-dimensional model. Since the simulation cannot be performed if the internal part of the inner plate is hollow, assume a composite

material as a combination of steel and a filler[21-23]. In this simulation, fitting length l = 250 mm, shrink fitting ratio $\delta/d = 0.2 \times 10^{-3}$, and friction coefficient μ = 0.3 are used as reference values. The shrink fitting ratio δ/d is defined as the shrink-fitted margin δ divided by the thickness d of the outer plate of the fitting portion (d = 240 mm).

In this study, since the inertial force can be ignored in the analysis[20], quasi-static structural analysis is performed by using FEM software MSC Marc/Mentat 2012 with the full Newton-Raphson method [31]. For contact analysis, a bilinear model based on the Coulomb friction model is applied [32]. A finite element model of Figure 3.1 is built to obtain the driving out force accurately within a short calculation time. A quadrilateral four-node element is used with a total mesh number is about 2.5×10^4, the calculation step is 0.0625s, and the minimum element size around the stopper is $0.15625mm \times 0.15625mm$.

As shwon in Figure 4, displacement of Point D, u_{xD} in different loading cycles under different load conditions (the reference condition is P = 1000N/mm, $\delta/d = 0.2 \times 10^{-3}$, μ = 0.3, l = 250mm) has been obtained as mentioned in Chapter 2. Here, Point D at 1.1 mm distance from the shrink-fitted surface is used to represent the contact point on the stopper. The number N_c denotes the cycle when the contact between the inner plate and the stopper starts as well as the stable status starts. When the load becomes large than the threshold P > 300 N/mm, the displacement u_{xD} increases with increasing N, then becomes stable after the inner plate contacts with the stopper. For example, when P = 1000 N/mm, the displacement reaches a constant value of 0.176 mm during the second cycle and does not change anymore. This is because reaching u_{xD} = 0.176 mm means that the point D contacts with the stopper [33]. With decreasing P, the contact starting cycle N_c increases, and when P is very small (P < 300N/mm), no contact occurs. This also indicates the reason why P = 1000N/mm is selected as the reference load to perform this study.

The contact force F_s appears when Point D of the inner plate and the around portion comes into contact with the stopper. Sometimes the inner plate does not come out and does not contact with the stopper depending on the analysis conditions. In these cases, the contact force F_s can be regarded as F_s = 0 for convenience. By considering the calculation time, the number of repeated loading cycle N=300 is used as the upper limit to judge whether the inner plate contacts with the stopper or not. The

detail will be described in Chapter 3.3.2. The driving out force will be calculated by the contact force

and the sum of the frictional shear forces of both shrink-fitted portions ($F_d = F_s = F_\tau^{up} + F_\tau^{down}$).

The model and the method of this research is for clarifying the coming out mechanism of the shaft

and the effect of design factors on the driving out force F_d. Three-dimensional real model should be

considered after clarifying the effect on the driving out force by two-dimensional model as a next

further study.

3.3 Effect of the Design Factors on the Driving out Force F_d

3.3.1. The Effect of Friction Coefficient μ

Figure 3.2 shows the frictional force acting on the upside F_τ^{up} and the frictional force acting on the

downside F_τ^{down} by varying the friction coefficient μ from $\mu=0.01$ to $\mu=1$. These friction shear forces

F_τ^{up} and F_τ^{down} are obtained by integrating the shearing stress τ_{xy} along the fitting length, as shown in

the following Equation (1):

$$\left. \begin{array}{l} F_\tau^{up} = \int_0^{250} \tau_{xy}^{up} dx \\ F_\tau^{down} = \int_0^{250} \tau_{xy}^{down} dx \end{array} \right\} \tag{1}$$
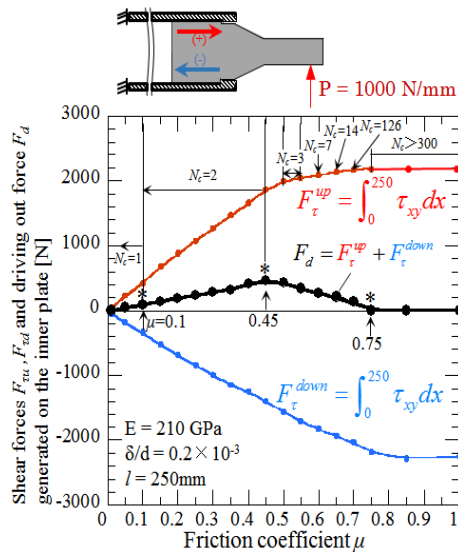
Figure 3.2 Shear forces F_τ^{up}, F_τ^{down}, and driving out force F_d generated on

the inner plate vs. friction coefficient μ.

In Figure 3.2, the positive shear force direction is defined in the x-direction as shown by the black arrow in Figure 3.1. Between the shear stress τ_{xy} and the contact normal stress σ_N, we have a relationship $\tau_{xy} = \mu \times \sigma_N$. The initial saturated contact number N_c when the inner plate and the stopper starts contacting with each other (see details in Figure 2.4) is also illustrated in Figure 3.2, and it helps us understand the effect of the friction coefficient on the coming out (coming out until the inner shaft is stopped by the stopper.) speed. When the coefficient of friction μ is less than 0.5, the coming out speed is almost the same, it takes the inner plate 1 or 2 loading cycles to go across the gap, then becomes contact with the outer plate. When the friction coefficient μ exceeds 0.5, with the increase of friction coefficient μ, the coming out speed suddenly becomes slow (when μ=0.7, N_c=126). The notation (N_c >300) in Figure 3.2 denotes no contact under the cycle N_c<300.

In Figure 3.2, the frictional shear forces F_τ^{up} , F_τ^{down} are depending on the friction coefficient μ. The driving out force F_d $(= F_\tau^{up} + F_\tau^{down})$ increases with increasing μ from $\mu = 0$ and takes a peak value around $\mu = 0.45$. This is because the shear force F_τ^{up} increases more steeply than F_τ^{down} increases and also because F_τ^{up} becomes saturated earlier than F_τ^{down} from the curve results. When μ becomes larger than μ=0.75, both shear forces F_τ^{up} , F_τ^{down} becomes saturated and balanced with each other numerically, and therefore F_d = 0. In other words, if μ becomes large enough, the inner plate cannot
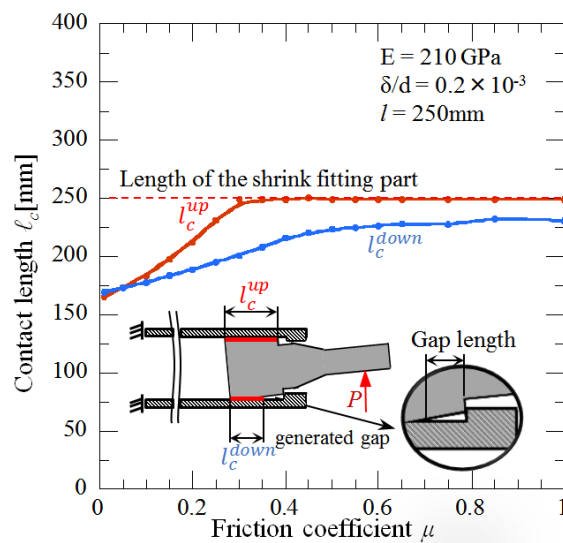
Figure 3.3 Contact length l_c^{up}, l_c^{down} between the inner plate (upside and downside) and the outer plate vs. friction coefficient μ.

move or come out into contact with the stopper anymore even when the bending load P is applied.

To understand the above discussion more efficiently, the contact length is examined between the inner and the outer plates. Figure 3.3 shows the contact length along with the upside l_c^{up} and along with the downside l_c^{down} of the inner plate when the upward load P is applied. Along the upside region, the whole length of shrink fitting portion $l = 250$ mm is almost contacted as $l_c^{up} = l = 250$ mm around $\mu = 0.3$. On the other hand, along the downside region, with increasing μ, the contact length l_c^{down} gradually increases until to $\mu = 0.6$ and becomes saturated as $l_c^{down} < 250$ mm.

Therefore, the downside shrink fitted length $l = 250$mm cannot contact along the whole length under upward loading. Note that the variations of l_c^{up} and l_c^{down} in Figure 3.3 are similar to the variations of F_τ^{up} and F_τ^{down} in Figure 3.2. This similarity suggests that the shear forces may be controlled by the contact length. This suggests that the contact lengths of both sides are related to the corresponding shear forces.

Note that l_c^{up} and l_c^{down} varies depending on the gap size generated during the coming out process as shown in Figure 3.2. Figure 3.4 shows the frictional shear stress distributions along both sides. Here, $\mu = 0.1$ is a small value of friction coefficient, $\mu = 0.75$ is a large value and $\mu = 0.45$ is
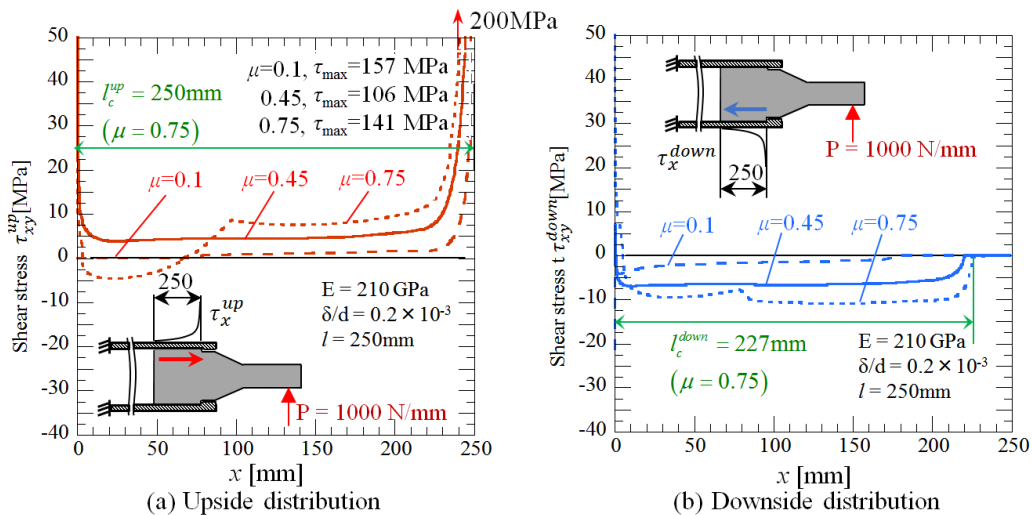
Figure 3.4. Shear stress distribution τ_{xy}^{up}, τ_{xy}^{down} along the upside and downside of the inner plate when $\mu = 0.1, 0.45, 0.75$

providing the maximum driving out force as shown in Figure 3.2. Those values are marked with asterisk* in Figure 3.2. When the upward load P is applied, the maximum shear stress appears at the upside right end (see Figure 3.4(a)) without a gap. On the contrary, the downside of the inner plate is stretched by the bending load P, and the gap appears between the inner and outer plates at the right end (see generated gap in Figure 3.3). Therefore, the contact length l_c^{down} in the range of $|\tau_{xy}| \neq 0$ is smaller than the contact length l_c^{up} over the entire friction coefficient range as shown in Figure 3.4 when the upward load P is applied.

Next, consider the friction coefficient μ providing to the maximum driving out force F_d . When μ is small, for example, $\mu = 0.1$, the shear forces on both sides are also small, and the sum of them $F_d = F_\tau^{up} + F_\tau^{down}$ is also small. When μ is significant, for example, $\mu = 0.75$, negative shearing stress τ_{xy}^{up} appears on the left side, the total shearing force F_τ^{up} cannot become larger. The driving out force $F_d = F_\tau^{up} + F_\tau^{down}$ decreases due to the negative shearing force F_τ^{down}. As a result, the driving out force F_d takes a peak value when $\mu = 0.45$, which is sandwiched between $\mu = 0.1$ and $\mu = 0.75$.

The relationship between the driving out force F_d and the friction coefficient μ, as shown in Figure 3.2, and the mechanism of the friction coefficient, are clarified for the first time in this study. It is desirable to avoid friction coefficient. $\mu = 0.45$, where the maximum value of driving out force is generated when designing the shrink-fitted roller. For example, under conditions where the coefficient of friction μ exceeds 0.75, there is no need to take into account the damage since no coming out occurs. However, since friction coefficient μ fluctuates due to practical environmental conditions, it is impossible to specify a specific friction coefficient μ as a design condition. Therefore, when designing an actual three-dimensional roller, it is sufficient to find the maximum value of the driving out force and based on this value for the strength design of the stopper. The behavior of the driving out force as shown in Figure 3.2 can be applied to the analysis and design of the three-dimensional real roller in the future.

3.3.2 The Effect of Shrink Fitting Ratio δ/d

The shrink fitting ratio δ/d is a key design factor for the shrink-fitted structure. A suitable value should be taken by considering the connected materials and applied torque appropriately. Figure 3.5 shows the relationship between the shrink fitting ratio δ/d and the driving out force F_d under the reference load P = 1000 N/mm. The first saturated contact number N_c is also shown in Figure 10, and it helps us understand the effect of the shrink fitting ratio δ/d on the coming out speed (coming out until the stopper stops the inner plate.). When shrink fitting ratio δ/d is less than 0.4, the coming out speed is almost the same, it only takes the inner plate 1 or 2 loading cycles to go across the gap, then becomes contact with the outer plate. When δ/d exceeds 0.4 (N_c = 66), with the increase of δ/d, the coming out speed suddenly becomes very slow (when δ/d ≥ 0.45, N_c > 300). When P = 1000 N/mm, the driving out force F_d is almost constant under the small fitting ratio $0 \leq δ/d \leq 0.2 \times 10^{-3}$. After that, F_d takes a peak value when δ/d ≅ 0.3×10^{-3} and F_d decreases significantly. This is because under a large shrink-fitting ratio δ/d, the inner plate cannot be driven out easily and results in F_d = 0 at δ/d = 0.45×10^{-3}. To confirm the relation between F_d and δ/d, the result for P = 1200 N/mm is also indicated in Figure 3.5. Similar tendency can be seen for P =1000 and P = 1200.

To investigate the effect of δ/d in detail, Figure 3.6 shows the shear stress distributions along the
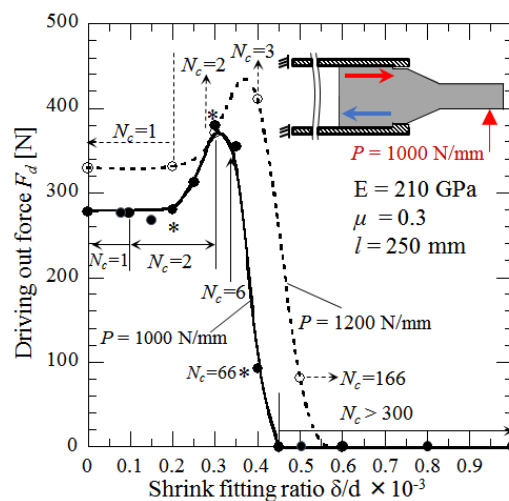
Figure 3.5 Driving out force F_d vs. shrink fitting ratio δ/d with different load conditions.

upside and downside shrink fitted portions. The driving force F_d can be expressed as the sum of those frictional forces as $F_d = F_\tau^{up} + F_\tau^{down}$ as mentioned above. Figure 3.6 focuses on the results of $\delta/d = 0.2\times10^{-3}$, 0.3×10^{-3} and 0.4×10^{-3}. Those values are corresponding to the results marked with asterisk* in Figure 3.5. As shown in Figure 3.5, the driving out force F_d takes the maximum value at $\delta/d \cong 0.3\times10^{-3}$, and F_d becomes smaller at $\delta/d = 0.2\times10^{-3}$ and $\delta/d = 0.4\times10^{-3}$. In Figure 3.6, when $\delta/d = 0.2\times10^{-3}$, the shear stress distributions τ_{xy}^{up}, τ_{xy}^{down} are smaller than the ones of $\delta/d \cong 0.3\times10^{-3}$ when F_d takes a peak value. Since τ_{xy}^{up}, τ_{xy}^{down} are smaller when $\delta/d = 0.2\times10^{-3}$, the sum of the forces F_d is also smaller. On the other hand, when $\delta/d = 0.4\times10^{-3}$, since the downside stress distribution τ_{xy}^{down} becomes larger than the upside stress distribution τ_{xy}^{up}, F_d becomes smaller.

The range of $\tau_{xy}^{up} \neq 0$ and $\tau_{xy}^{down} \neq 0$ in Figure 3.6 area contact regions where shearing stress is generated by contact. Figure 3.6(b) illustrates that as the fitting ratio δ/d increases, l_c^{down} also becomes longer until the inner plate completely contact with the outer plate. From a different point of view, it is thought that the smaller the non-contacting part that occurs on the opposite side due to
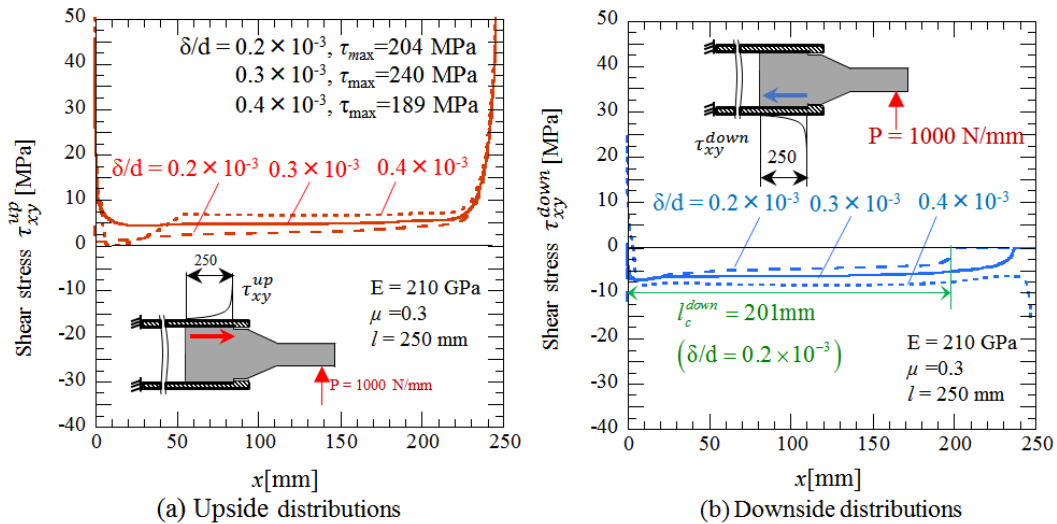
Figure 3.6 Shear stress distribution τ_{xy}^{up}, τ_{xy}^{down} along both sides of the inner plate when the shrink fitting ratio δ/d is different.

the bending load, the more deformation of the inner plate is restrained and the more difficult it is to

come out. Thus, the fact that l_c^{down} does not become short even when an upward bending load P is

applied under a larger fitting ratio δ/d is also a factor that makes the coming out difficult.

Here, the number of repetitions of the loading cycle N required to calculate the driving out force

F_d under the bending load P = 1000 N/mm is described concerning the fitting ratio δ/d next. Figure

3.7 shows the relationship between the displacement u_{xD} of the inner plate and the number of loading

cycle N under different shrink fitting ratio δ/d. As shown in Figure 3.7, for small δ/d, the

displacement u_{xD} becomes constant only after several cycles N_c. For example, when δ/d = 0.2 × 10^{-3},

the contact appears at N_c = 2. When δ/d = 0.4 ×10^{-3}, the contact appears at N_c = 66. It should be

noted that the contact displacement is smaller than the initial gap of 0.2 mm because the

contact condition should be taken as the value more than half of the shrink fitting ratio δ/d as the

determination amount. Therefore, u_{xD} in the stable contact state when δ/d = 0.4 ×10^{-3} is smaller than

the u_{xD} when δ/d = 0.2 × 10^{-3}. For a much larger value of δ/d = 1.0 × 10^{-3}, the displacement u_{xD}

hardly increases and therefore no contact anymore under N =300 cycles. To reduce the calculation

time, in this study, no contact under N=300 is regarded as the zero driving force F_d =0 as the same

as mentioned in advance in section 2. Therefore, from Figure 3.5, the shrink fitting ratio δ/d = 0.45

can be regarded as the threshold contact value.
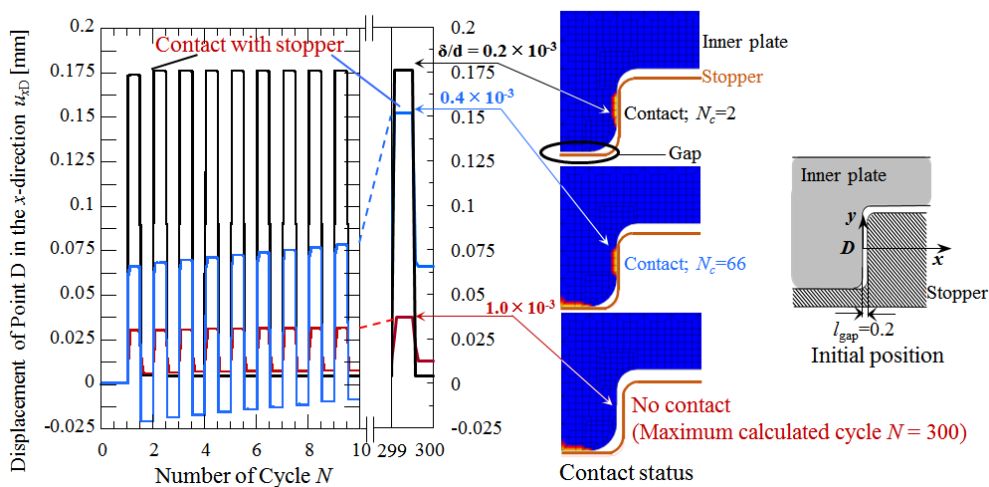
Figure 3.7 Displacement of point D u_{xD}vs. different shrink fitting ratio δ/d when P = 1000 N/mm; E = 210 GPa; μ = 0.3, l=250mm.

The unique behavior of the driving out force F_d depending on the fitting ratio δ/d, which was first clarified in this study as shown in Figure 3.5, can be considered as similar to the case of the friction coefficient μ. Therefore, as in the case of the discussion of μ, the application to an actual three-dimensional design is to obtain the maximum F_d and conduct the strength design for the stopper. However, considering the ceramic sleeve's brittleness, the condition of 0.3×10^{-3} or less in fitting ratio should also be added. In this way, the behavior of the driving out force as shown in Figure 3.5 can be applied to the analysis and design of the three-dimensional real roller in the future.

3.3.3 The Effect of Fitting Length *l*

Figure 3.8 shows the effect of the shrink fitting length *l* on the driving out force F_d . The ratio of *l*/d is also illustrated in Figure 3.8. Similarly, Figure 3.8 also shows the initial saturated contact number N_c, and it helps us understand the effect of the fitting length on the coming out speed (coming out until the inner shaft is stopped by the stopper.). When the fitting length *l* is less than 200 mm, the speed is the same with each other ($N_c = 1$), when *l* reaches 250 mm, N_c =2, and when *l* exceeds 350 mm, with the increase of *l*, the coming out speed suddenly becomes very slow (when $l = 390, N_c = 50$).   Except for extremely short fitting length, the driving out force F_d is
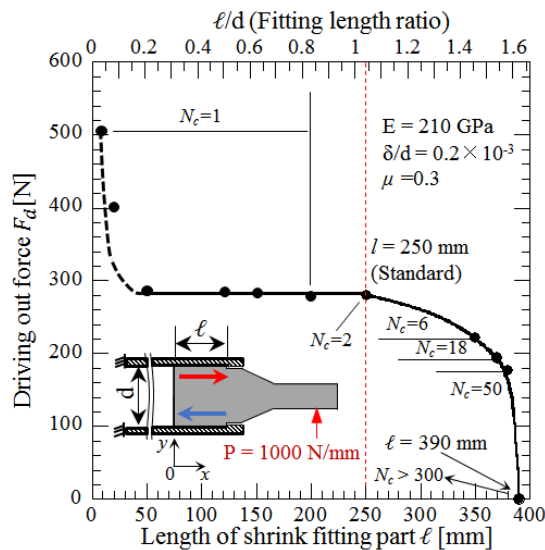
Figure 3.8 Driving out force F_d in the *x*-direction vs. shrink fitting length *l*

almost constant for small length in the range $0.5 \leq l/d \leq 1.0$, that is, 120 mm $\leq l \leq$ 250mm. When $l/d >$ 1.0, the driving out force F_d gradually decreases with increasing l/d.

As described above, the longer the fitting portion is, the harder it is for the inner plate to come out, but it is also necessary to consider that when the fitting portion is too long, it will reach to the inside of the high-temperature furnace and an increase in cost. On the other hand, when the fitting length ratio $l/d \leqslant 0.2$, the driving out force increases, but in an actual design it is difficult to assume in l/d <0.5, and therefore, empirically set $l/d = 0.25 \sim 1$. Therefore, when designing a three-dimensional real roller, the driving out force can be calculated using the fitting length ratio $l/d = 0.5 \sim 1.0$ with a substantially constant driving out force as a guide, and it can be used for the strength design of the stopper. In this way, the behavior of the driving out force as shown in Figure 3.8 can be applied to the analysis and design of the three-dimensional real roller in the future.

3.3.4 The effect of Young's modulus of the inner plate

Figure 3.9 shows the effect of Young's modulus of the inner plate on the driving out force F_d for $E_{in} / E_{in}^{\text{standard}} = 0.25 \sim 4.0$. Here, E_{in}^{standard} denotes Young's modulus of the standard inner plate, which
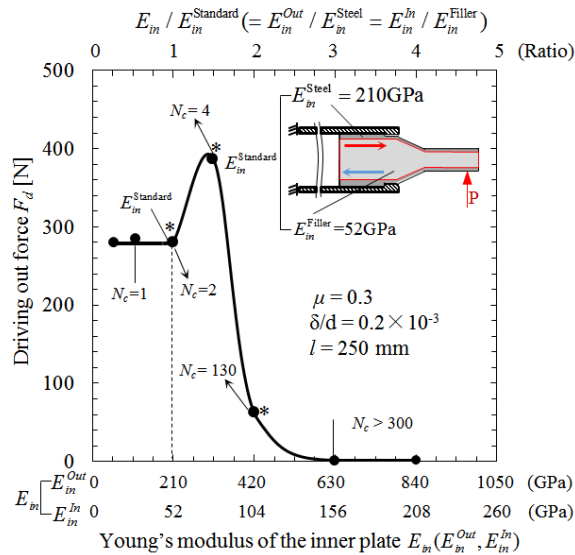
Figure 3.9 Driving out force F_d in the x-direction vs. Young's modulus of the inner plate

is composed of the steel outer layer with $E_{in}^{Out} = E_{in}^{Steel} = 210$ GPa and the filler inner portion with $E_{in}^{In} = E_{in}^{Filler} = 52$ GPa. In Figure 3.9, the driving out force F_d is indicated depending on $E_{in}/E_{in}^{standard}$. The horizontal axis also shows E_{in}^{Out} and E_{in}^{In}. In this study, the same ratio $E_{in}/E_{in}^{standard} = E_{in}^{Out}/E_{in}^{Steel} = E_{in}^{In}/E_{in}^{Filler}$ is assumed.

During $E_{in}/E_{in}^{standard} = 0.25 \sim 1$, driving out force F_d is almost constant and takes a peak value at $E_{in}/E_{in}^{standard} = 1.5$. With increasing $E_{in}/E_{in}^{standard}$ more, the coming out becomes difficult because the driving force F_d dramatically decreases to $F_d = 0$ when $E_{in}/E_{in}^{standard} \geq 3$. Likewise, Figure 14 also shows the first saturated contact number N_c, and it helps us understand the effect of Young's modulus of the inner shaft on the coming out speed (coming out until the inner shaft is stopped by the stopper.). When Young's modulus of the inner shaft $E_{in}/E_{in}^{standard} \leq 1.5$, the speed increases slowly (when $E_{in}/E_{in}^{standard} \leq 0.5$, $N_c = 1$; when $E_{in}/E_{in}^{standard} = 1.5$, $N_c = 4$;), when $E_{in}/E_{in}^{standard} = 2$, $N_c = 130$, and when $E_{in}/E_{in}^{standard} \geq 3$, $N_c > 300$.

To explain the variation tendency, three conditions marked with asterisk* in Figure 3.9 are selected to be investigated. Figure 3.10 illustrates the shear stress distributions along the shrink

(a) Upside distributions

(b) Downside distributions
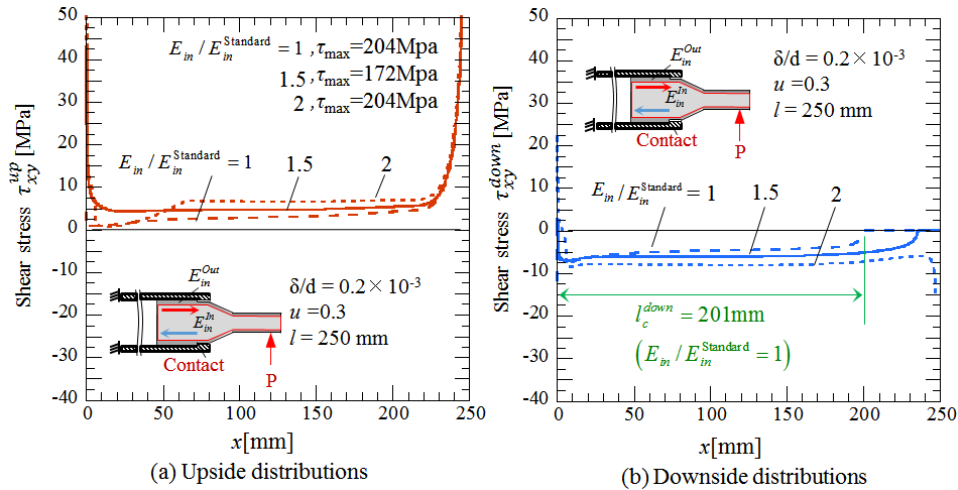
Figure 3.10 Shear stress distributions τ_{xy}^{up}, τ_{xy}^{down} along both sides of the inner plate depending on different Young's modulus E_{in}.

fitting portions corresponding to those asterisk* points. The shear stress distributions τ_{xy}^{up}, τ_{xy}^{down} for

standard Young's modulus $E_{in}/E_{in}^{\text{standard}}=1$ is smaller than the shear stress distributions $\tau_{xy}^{up}, \tau_{xy}^{down}$ at

$E_{in}/E_{in}^{\text{standard}}=1.5$ where the maximum F_d appears. This is the reason why F_d at $E_{in}/E_{in}^{\text{standard}}=1$

is smaller than F_d at $E_{in}/E_{in}^{\text{standard}}=1.5$ since F_d is the sum of frictional forces. On the other hand,

when $E_{in}/E_{in}^{\text{standard}}=2$, the negative shear distribution τ_{xy}^{down} along the downside becomes much

larger than the positive shear distribution τ_{xy}^{up} along the upside. This is the reason why the sum of

frictional forces F_d at $E_{in}/E_{in}^{\text{standard}}=2$ is smaller than F_d at $E_{in}/E_{in}^{\text{standard}}=1.5$. When

$E_{in}/E_{in}^{\text{standard}} \geq 3$, the displacement does not increase and therefore no coming out appears anymore

with increasing the cycle loading N.

The effect of Young's modulus E_{in} of the inner plate in Figure 3.9 is similar to the effect of the

shrink fitting ratio δ/d in Figure 3.5 since both figures show similar variations. With increasing the

shrink fitting ratio δ/d, the fitting pressure increases. This is equivalent to increasing Young's

modulus of the inner plate. From this results, theoritically it is recommended that the inner plate has

more than twice larger than the standard Young's modulus as shown in Figure 3.9. But in practice, it

is necessary to obtain the maximum F_d by and applied it to the strength design of the stopper. In

this way, the behavior of the driving out force as shown in Figure 3.9 can be applied to the analysis

and design of the three-dimensional real roller in the future, which will never be found out without

this study.

3.4 Conclusions

In this study, in terms of the shrink-fitted roller, the effects of various design factors on the coming

out of the shaft from the ceramic sleeve was considered. Specifically, before the analysis of the

three-dimensional real roller model, the two-dimensional FEM model shown in Figure 2.2, 2.3 is

used to investigate the effects of the friction coefficient $μ$, the fitting length l, and the shrink fitting

ratio δ/d on driving out force F_d. In a two-dimensional model, it is possible to realize the number

of loading cycles required to determine F_d in about 1/120 of computation time, and to analyze this

relatively complicated mechanism in a relatively easy way. Therefore, elucidation of the individual

behavior of each design factor with respect to the driving out force with a two-dimensional model is essential in advancing analysis before the consideration of a three-dimensional real roller model. The conclusions can be summarized in the following way.

(1) The effect of the friction coefficient μ on driving out force F_d was shown to exhibit the unique behavior as shown in Figure 3.2. That is, as μ increases from $\mu = 0$, F_d gradually increases, but reaches a maximum value near $\mu = 0.45$ and then gradually decreases until $F_d = 0$.

(2) The effect of the fitting ratio δ/d on driving out force F_d was shown to exhibit the unique behavior as shown in Figure 3.5. That is, when δ/d is small, F_d takes an almost constant value, but when δ/d increases, F_d reaches a maximum value near δ/d $= 0.3 \times 10^{-3}$ and then sharply decreases to 0 near δ/d $= 0.45 \times 10^{-3}$.

(3) As shown in Figure 3.8, the effect of the fitting length ratio l/d on driving out force F_d was found to be different from (1) and (2). That is, when l/d increases from 0, it decreases rapidly and then keeps a constant value from around l/d = 0.2, but when l/d exceeds around 1.0, it starts to drop, near l/d = 1.6, F_d reaches to 0.

(4) The effect of the Young's modulus of the shaft E_{in} on driving out force F_d was shown to exhibit the unique behavior as shown in Figure 3.9. That is, when E_{in} is small, F_d takes an almost constant value, but when δ/d increases, F_d reaches a maximum value near $E_{in} / E_{in}^{\text{standard}} = 1.5$ and sharply decreases to 0 near $E_{in} / E_{in}^{\text{standard}} = 3$.

(5) When designing a three-dimensional real roller, the maximum value of the driving out force F_d should be acquired based on the behavior clarified in this study, and used for the strength design of the stopper. Thus, the knowledge obtained by this two-dimensional model analysis can be applied to the analysis of the three-dimensional model in the future for next procedure and to the design of the stopper structure that receives the driving out force F_d .

3.5 References of Chapter 3

Chapter 3

[1]   R. P. Larsen and A. D. Vyas: Proc. SAE Int. Cong. and Exp, SAE Technical Paper, Dearborn, MI, Sep.**1988**

[2]   P. Wray, *Advanced Structural Ceramics*, Tech Monitoring, SRI International, Japan, **1991**.

[3]   S. Jahanmir, *Friction and Wear of Ceramics*, Marcell Dekker, New York, **1994**.

[4]   U. Dworak, in *High-tech Ceramics "Viewpoints and perspectives"*, (Eds: K. Gernot), Academic Press Limited, London, **1989**.

[5]   S. Sen, B:Aksakal, *Mater & Des.* **2004**, *25*,407.

[6]   M. Fujii, A. Yoshida, J. Ishimaru, S. Shigemura, K. Tani, *Trans. Jpn. Soc. Mech. Eng. C*. **2006**, *72*, 1354.

[7]   C. Liour, T. Mori, H. Kobayashi, T. Mitamura, *JCS-Jpn*. **1990,** *98*, 348.

[8]   T. Ono, *J. Jpn. Soc. Mech. Eng*. **1983**, *86*, 470.

[9]   W. Li, N.A. Noda, H. Sakai, Y. Takase, *J. Solid Mech. Mater.Eng*. **2011,** *5*, 14.

[10]   W. Li, N.A. Noda, H. Sakai, Y. Takase: *Key Eng. Mater*. **2011,** *452*, 241.

[11]   A. Rusin, G. Nowak, and W. Piecha: *Engi. Fail. Anal*. **2013**, *34*, 217.

[12]   M.Tsuyunaru, N.A. Noda, Hendra, Y. Takase: *Trans. Jpn. Soc. Mech. Eng. A*. **2008**, *74*, 919.

[13]   N.A. Noda, Hendra. Y. Takase, M. Tsuyunaru, *J. Solid Mech. Mater.Eng*. **2008**, *2*, No.2, 1410.

[14]   N.A. Noda, M. Yamada, Y. Sano, S. Sugiyama, S. Kobayashi: *Engi. Fail. Anal*. **2008**, *15*, 261.

[15]   N.A. Noda, Hendra, M. Oosato, K. Suzumoto, Y. Takase, W. Li, *Key Eng. Mater*. **2011**, *462*, 1140.

[16]   S. Matsuda, D. Suryadi, N.A. Noda, Y. Sano, Y. Takase, S. Harada, *Trans. Jpn. Soc. Mech. Eng. A*. **2013**, *79*, 989.

[17]   E. Ogawa, K. Shimizu, S. Hamayoshi, N. Kumagai, Y. Ohtsubo, N.A. Noda, Y. Takase, K, Kishi, K. Shobu, T. Tabaru, E, Maeda, S. Koga, T. Matsuda: *Hitachi Metals Tech.Rev*. **2012**, *28*, 50.

[18]   N.A. Noda, D. Suryadi, S. Matsuda, Y. Sano, Y. Takase, *ISIJ In*. **2015,** *55*, 2416.

[19]   S.Harada, N.A.Noda, O.Uehara and M.Nagano, *Trans. Jpn. Soc. Mech. Eng. A*. **1991,** 57, 1637.

[20]   N.A. Noda, D. Suryadi, S. Kumasaki, Y. Sano, Y. Takase, *Engi. Fail. Anal*. **2015**, *57*,219.

[21]   N.A. Noda, Y. Xu, Y. Sano, Y. Takase, *ISIJ Int*. **2016,** *56*, 303.

[22]   G. Zhang, H. Sakai, N.A. Noda,Y.Sano and S. Oshiro, *ISIJ Int*. **2019**, *59*,No.2,293.

[23] N.A. Noda, Y.Sano, Y.Takase, S.Harada, D.Suryadi, S. Kumasaki, *Tetsu-to-Hagané*. **2015,** *101*, 10,(in Japanese).

[24] Y.Sano, H.Sakai, G. Zhang, N.A Noda, 6th Int.Conf. on Fracture Fatigue and Wear, IOP Publishing, Bristol, May, **2017**.

[25] T. Miyazaki, N.A. Noda, F. Ren, Z Wang, Y. Sano, K.Iida, *Int J Adhes Adhes*. **2017**, *77*,118.

[26] N.A. Noda, T. Miyazaki, R.Li, T. Uchikoba , Y. Sano, *Int J Adhes Adhes*. **2015,** *61*, 46.

[27] N.A. Noda, T.Uchikoba, M.Ueno, Y. Sano, K. Iida, Z.Wang, G.Wang, *ISIJ Int*. **2015**, *55*, 2624

[28] Z .Wang, N.A. Noda, M. Ueno,Y. Sano, *Steel Res Int*. **2016**, *88*, 353.

[29] N.A. Noda, Y.Shen, R. Takaki, D. Akagi, T. Ikeda, Y .Sano and Y. Takase, *Theor Appl Frac Mec*. **2017**, *90*,218

[30] N.A. Noda, X. Chen, Y. Sano, M.A. Wahab, H. Maruyama, R. Fujisawa, *Mater&Des*. **2016**, *96*,476

[31] Marc Mentat team, Theory and User Information. Vol.A, MSC.Software. Tokyo, **2012**. 713.

[32] Marc Mentat team, Theory and User Information. Vol.A, MSC.Software. Tokyo, **2012**. 545.

[33] Marc Mentat team, Theory and User Information. Vol.A, MSC.Software. Tokyo, **2012**. 572.

Chapter 4 Failure mechanism of the coming out of steel shaft from ceramic sleeve and calculation of the driving out force by three-dimensional finite element model

4.1 Introduction

Figure 4.1 shows the heating furnace where the steel conveying rollers are used to produce high-quality steel plates. Figure 4.2 shows three-dimensional roller structures traditionally used and a new roller which have been developed recently. Figure 4.2(b) introduces a new roller consisted by steel shafts at both ends and ceramic sleeve by shrink fitting method, which overcomes some imperfections of the conventional roller as shown in Figure 4.2(a). For example, since the thermal expansion coefficient of steel is four times of the ceramics, the thermal expansion mismatch may fertilize surface failure such as wearing, crack, peeling leading to short roller life [1] though the steel sleeve is coated by ceramics on the surface. In addition, adhesive and metal bonding can not satisfy the strength requirement under elevated temperature.

Similar ceramic structures as this new roller under high temperature environment in the continuous pickling line [2], the heating furnace [3], and in continuous galvanizing line [4] have been considered
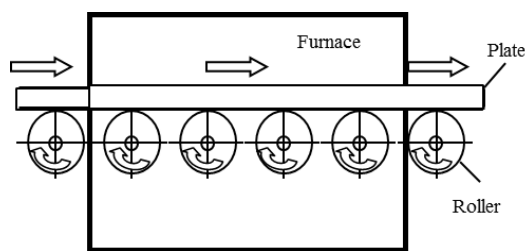

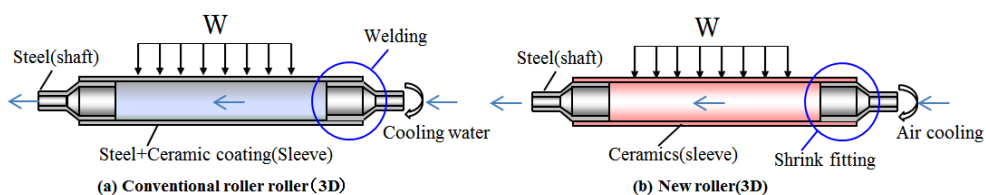Figure 4.1 Layout of rollers in a kind of heating furnace

Figure 4.2 Roller structures (a) Conventional roller (b) New roller

in previous studies. It is suggested that the shrink fitting may be the most suitable connection method for cylindrical ceramic and the maintenance cost as well as reducing replacement time of the shaft. However, a word of caution that only low shrink fitting ratio can be applied for those structures because of the ceramic brittleness is necessary. Meanwhile, for a slender roller structure, especially operated under elevated temperature, once both ends are fixed, it may be broken easily because of no allowance for large axial thermal deformation. Since the axial movement of the shaft can not be constrained by the bearings of the free end for the rollers, the coming out can be problematic. Even when the shaft movement is restricted within a small allowable range, the coming out of the shaft (relative slide on the shrink fitting surdace) may cause local thrust loading, frictional heat generation, and wear, which will acceralate the failure of the roller. And the coming out phenomenon of the shaft was observed in small prototype rollers [5] in the rotating bending experiment by Ono rotary bending fatigue testing machine [6]. It also validated that the analytical simulations by finite element method is suitable [5].

Previously, for some other shrink-fitted structures, Booker and Truman investigated micro-slipping problem between the gear hub and shaft connected by shrink fitting [7]. Antony analyzed contact separation failure for rotating thermos-elastoplastic shrink-fitted assembly [8].

In recent years, to prepare for this new failure of coming out of the ceramics sleeve roller, a series of studies [5,9] were performed. The coming out simulations are conducted by using the finite element method [5, 9] which is one of the most used numerical modeling techniques. In the first place, Suryadi [5] et.al built an actural three-dimensional FEM model as shown in Figure 4.2(b) and performed the coming out simulation by load shifting method. Although the fundamental coming out failure analysis was conducted, the computation time was too large to get sufficient loading circles. To predict the coming out behavior more accurately, the simplified two-dimentional model was considered as is shown in Figure 4.3 (a) Xu [9] et.al developed two-dimensional model to reduce the calculation time and obtained the results when number of cycle N is larger than 10. Those studies [5, 9] have proved that the coming out behavior can be realized by the two-dimensional and three-dimensional simulations, and some proposals have been raised. To find the mechanism of the coming out of the shaft from the

ceramic sleeve further, in this study, in Chapter 2 and Chpter 3, a novel stopper installing on the outer plate of the two-dimentional model as is shown in Figure 4.3(b) was designed. The comging out process was illustrated and the coming out mechanism was clarifed as is shown in Figure 4.4, where the reaction force generated at the stopper can be regarded as the driving out force F_d and the magnitude was obtained under the reference condition. To design the fitting parts of the two-dimentional roller with a lower F_d, the effects of several fundamental design factors on F_d were investigated. As an example, the effect results shows that the effect of Young's modulus of the shaft and the effect of shrink fitting ratio on the driving out force are almost the same, but the effect of the peak value is relatively small in both cases.

These studies inspired the authors to explore the coming out mechanism and to calculate the driving out force F_d for actual three-dimensional model. In this study, finite element method is adopted to perform the numerical analysis by using the commercial software, MSC.MARC 2012. A novel Ball-stopper designed for the three-dimensional model originally to fertilize the mechanism analysis and calculation of F_d will be introduced.

(a) 2D model without stopper for coming out phenomenon analysis

(b) 2D model with stopper for coming out mechanism analysis and calculating the driving out force F_d

(c) Alternate loading applied on the 2D models (a) and (b)

(d) Detail of stopper (S)
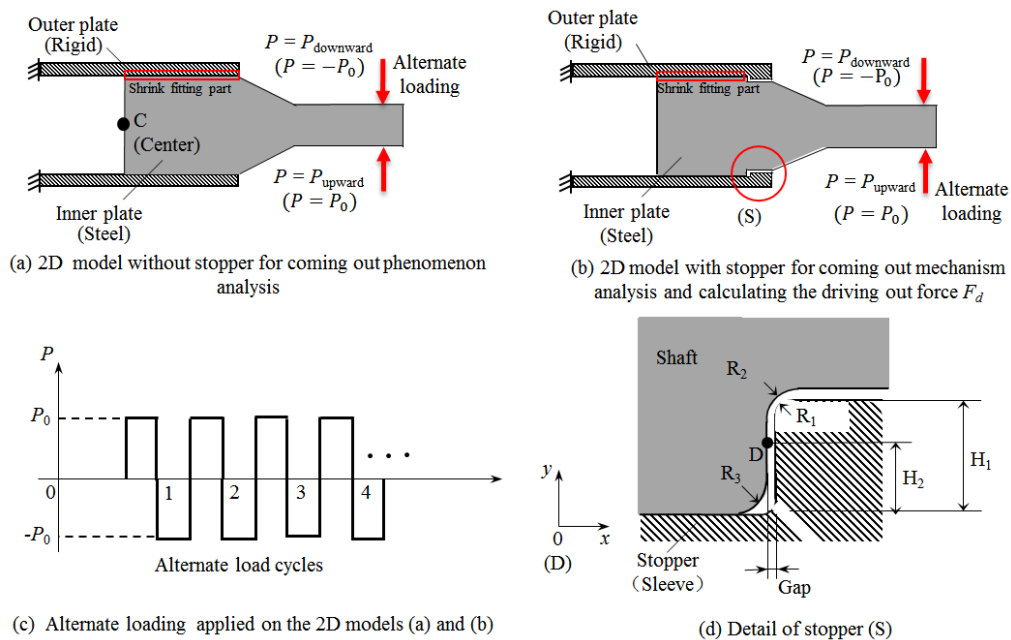
Figure 4.3 Simplified 2D models (a) 2D model without stopper (b) 2D model with stopper considered in the previous paper [5]

4.2.Analysis method

4.2.1 New analysis model with Ball-stopper

4.2.1.1 The new Two-dimensional model with a Ball-stopper

In terms of previous two-dimentional model as is shown in Figure 4.3(a) and (b), a stopper to accept the driving out force F_d and to help to clarify the coming out mechanism are introduced. The results indicated that this is a effective way to analyse the coming out failure mechanism and calculated F_d. It should be noted that it is much more difficult to build a three-dimentional model even without such a kind of inner stopper to balance the convergence accuracy and the computation time. Here, to build the three-dimentional model with a delicate stopper structure along the circumferential of the sleeve is not easy, especially for meshing and convergence in term of the contact problem. Therefore, there is an urgent need for a much more convenient approach to realize the function just as the stopper in two-dimensional model.

Here, a Ball-stopper approach for realizing this will be originally introduced. Set a newly designed Ball-stopper outside the roller for accepting the driving out force with a small scale distance (i.e.like the gap in two-dimentional model in Figure 4.3(d)) from the end edge of the shaft). Before that, a Ball-stopper for two-dimentional model analysis should be performed in the first place to confirm if the results obtained are consistent with the previous one's results as mentioned in Chapter 2 and Chapter 3. As is shown in Figure 4.5, a new Ball-stopper plate is designed for the two-dimentional
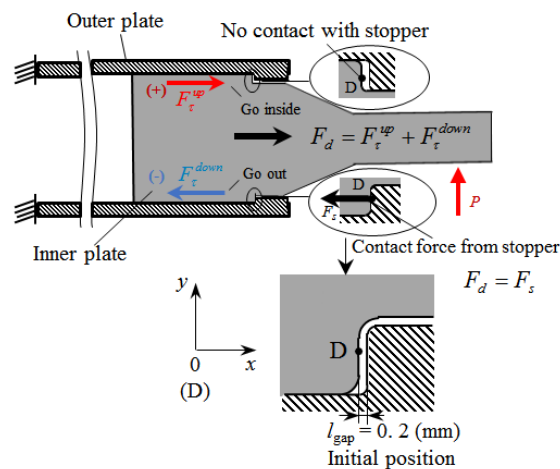
Figure 4.4 Generation mechanism of the driving out force F_d balanced with the reaction F_s at the stopper.

model and it is placed in front of the two-dimentional model without inner stopper. To make the calculation easier and more accurate, we assume the contact between the right edge of the inner plate and the two-dimentional Ball-stopepr as rigid contact for easy collecting the driving out force data. The rigid part of the inner palte and its rest part as assumed as perfectly bonded together when specifying the contact type as is shown in Figure 4.5.

The reference condition was the same as the refenence condition performed in Chapter 2 and Chapter 3, where the alternate load P =1000 N/mm, shrink fitting ratio is $\delta/d = 0.2\times10^{-3}$, friction coefficient is $\mu = 0.3$. The material properties is listed in Table 4.1. A quadrilateral 4 node element is used with a total mesh number is about 2.7×10^{4}, the minimum element size around the apex of the hemisphere Ball-stopper is 0.7 mm $\times$ 0.5 mm. Quasi-static structural analysis [10] was conducted by using FEM software MSC Marc/Mentat 2012 with the full Newton-Raphson method. For contact analysis, a bilinear model based on the Coulomb friction model was applied [11]. Figure 4.6 shows the driving out force obtained by Stopper model (see Figure 4.3(b)) and Ball-stopper model of Figure 4.5 under the reference condition. They were found to be almost the same with each other within 6% difference. Therefore, this Pin-Ball approach may have good potential to apply on three-dimentional model.
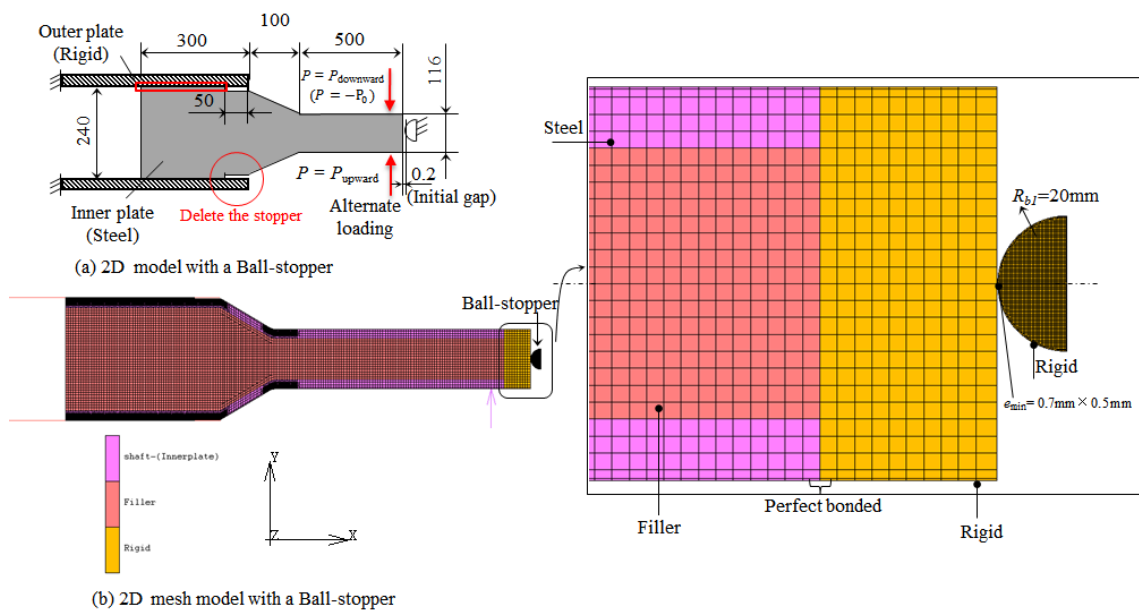
Figure 4.5 The newly designed two-dimensional model with a Ball-stopper

4.2.1.2 The new design of the three-dimensional model with a Ball-stopper

Figure 4.7 shows the actual three-dimentional roller model. Figure 4.8 shows the new analysis half three-dimensional model with the Ball-stopper and the FEM model with boundary conditions. Table 4.2 shows the mechanical properties of the materials of the three-dimentional model with a rigid Ball-stopper. The material of the sleeve is silicon nitride. The shaft is made of the relatively inexpensive but tough enough alloy steel. The right end edge of the shaft structure should be changed from hollow into solid, and the material is better to be rigid. Likewise, to reduce the computation time and to obtain the results more accurate, we assume the contact between the right edge of the shaft and the Ball-stopper (3D) as rigid contact for easy collecting the driving out force data. The rigid part of the shaft at the right end is assumed as perfectly bonded with the rest part of

Table 4.1. Material properties of the two dimentional model with a Ball-stopper

	Outer plate	Inner plate		Ball-stoppe(2D)
Material	Rigid*	Steel	Filler*	Rigid*
Young's modulus [GPa]	∞	210	52	∞
Poisson's ratio	—	0.3	0.3	—
Tensile strength [MPa]	—	600	—	—
Mass density [kg/m^3]	—	7800	7800	—

*Assumed in the simulation.
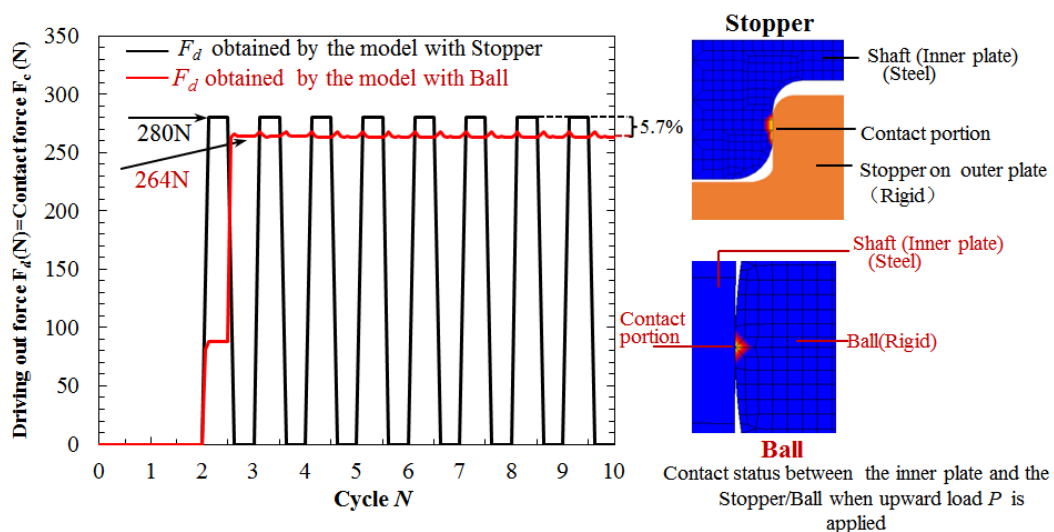
Figure 4.6 Driving out force F_d abtained by Stopper model (See Figure 4.3(b))vs driving out force obtained

the shaft when specifying the contact type as is shown in Figure 4.8. The friction model has to be specified when the contact calculation is performed. In terms of MSC Marc/Mentat 2012, it has been told that the Coulomb friction model can be widely used for most practical applications except for bulk forming as encountered in e.g. forging processes. The arctangent model, stick-slip model and bilinear model are aviliable [11]. However, the arctangent model is unsuitable for estimating the typical relative sliding velocity priori when the sliding velocity varies largely during the analysis. Also, the stick-slip model needs a large amount of data to be determined from repetitive calculation process [11]. In this paper, therefore, to avoid the huge computation time, the bilinear model is applied since the friction force is simply determined from the displacement.

Table 4.2. Material properties of the three-dimentional model with a Ball-stopper

	Sleeve	Shaft	Ball-stopper(3D)& Right edge of the Shaft
Material	Ceramic	Steel	Rigid
Young's modulus [GPa]	300	210	∞
Poisson's ratio	0.28	0.3	—
Tensile strength [MPa]	500	600	—
Mass density [kg/m^3]	3200	7800	—
Thermal expansion coefficient[1/K]	0.3×10^{-5}	1.2×10^{-5}	—

$\delta/d=0.2\times10^{-3}$
$\mu =0.3$
$v= 0.28$
$\rho =3200$ kg/mm^3
$E_{sl}=300$GPa
$E_{sh}=210$GPa
$w = 30$N/mm
$t =20$mm
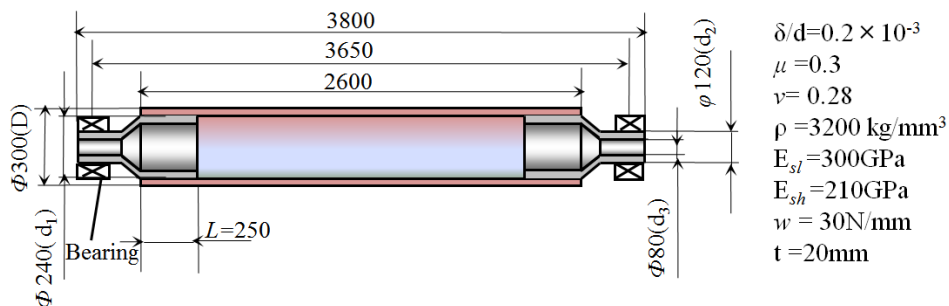
Figure 4.7 Structure and dimensions of the new roller model with standard dimensions (mm) (3D)

Generally, inertial force effect during the roller rotation should be considered. Since the inertial force can be neglected in analysis calculated by Dedi et al. because of its extremly small error [ ], which means due to the inertial force effect, the inner radius of the ceramic sleeve may expand only 2.94×10^{-5}mm [5] along the radial direction, then the shrink fitting ratio may be reduced by only 0.12% [5], a quasi-static simulation with the method of load shifting [5] as is shown in Figure 4.9 will be performed. The continuous load shifting can be replaced by discrete load shifting with a load shift angle θ_0. It is usually used as a standard discretization numerical analysis. To select a proper shift angle θ_0, change θ_0 from 6° to 12°, 18° and 30°, focused on the coming out displacement of point C, since the effect of discrete load shifting is less than 1% if $\theta_0 \leq 12°$, it may be the most suitable load shifting angle to reduce huge calculation time without losing accuracy[5]. The standard simulation condition is load $w = 30$ N/mm, shrink fitting ratio is $\delta/d = 0.2 \times 10^{-3}$, friction coefficient is $\mu = 0.3$.
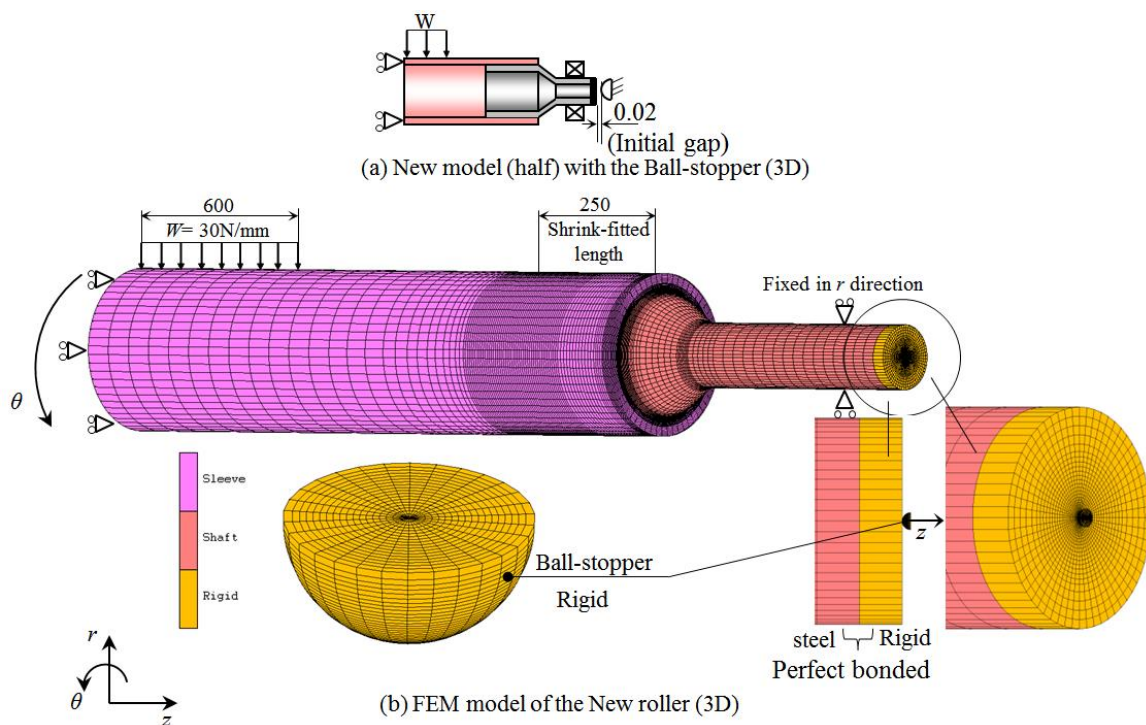
Figure 4.8 New model (half) with the Ball-stopper and the FEM model

4.3 The mechanism of the coming out failure and the calculation of the driving out force

In Chapter 2 and Chapter 3, with the help of the novelly designed stopper installing on the outer plate of the two-dimentional model as is shown in Figure 4.3(b), the mechanism of the coming out of the inner plate (shaft) from the ceramic sleeve as is shown in Figure 4.5 is clarifed. The inner plate comes out gradually when the alternate loading is applied, goes across the gap between the inner plate and the stopper and finally contacts with the stopper. The reaction force F_s appears at the stopper can be regarded as the driving out force F_d exactly. A kind of driving out force F_d must have been generated and be acting on the inner plate (shaft). Then, the driving out force F_d is balanced with the resultant frictional forces F_τ^{up} and F_τ^{down} appeared along both sides of the fitting portions that is, $F_d = F_\tau^{up} + F_\tau^{down}$. Once the inner plate moves forward, the inner plate cannot be recovered to the original position even after the load is removed. This residual displacement is accumulated and the inner plate gradually comes out. And the coming out simulation was numerically realized within much less time by applying the alternate loads.

Regarding the three-dimentional real model simulation, assuming that it behaves similar as the two-dimentional model and they have similar coming out mechanism. Then the driving out force (contact force F_s) F_d and the frictional shear forces $F_\tau^{resultant}$ should be calculated out to check whether they satisfy the $F_d = F_\tau^{resultant}$. $F_\tau^{resultant}$ is distributed on the inner cylinder surface. It is found only the vertex of the hemisphere Ball-stopper, Point R has contacted with the shaft, which is also expected for convenient results collecting. The contact force F_s of Point R along the comging out dircetion (z-direction) betwee the shaft and the Ball-stopper caused by the driving out force F_d is a reaction force
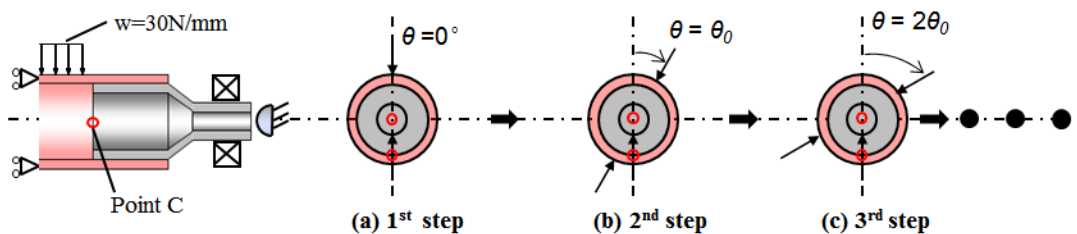
Figure 4.9 The load shifting method

of F_d, they have the same magnitude. Therefore, F_d can be obtained by F_s. To make sure the accuracy of the contact result, the loading shift angle θ_0 has been selected as 12° previously. The new part compared with the previous model, that is the Ball-stopper, should also be checked for selecting a good expand angle for computation accruracy.

Figure 4.10 shows the driving out force obtained by the aforementioned FEM model with different Ball-stoppers whose expand angle θ are 12°,10°and 6° respectively (Ball-stopper 1, Ball-stopper 2, Ball-stopper 3). The solid lines show that F_d almost varies almost the same when the expand angle $\theta =$ 10° and 12°. The dash line shows there is no large difference with the solid line results when $\theta = 6°$, but the aspect ratio of the linear hexahedron element is relative large. To reduce the mesh number and to avoid a large element aspect ratio, $\theta =12°$ is selected as the standard expand angle for further calculation.

The driving out forces F_d initially increase then become stable after 3 cycles due to contact with the Ball-stopper, and then keeps stable. The magnitude is almost proportional to the load magnitude. Table 4.3 shows that the driving out forces F_d are almost balanced with the frictional forces $F_\tau^{resultant}$ obtained from the inner cylinder surface which are in contact status with the shaft by Ball-stopper 3
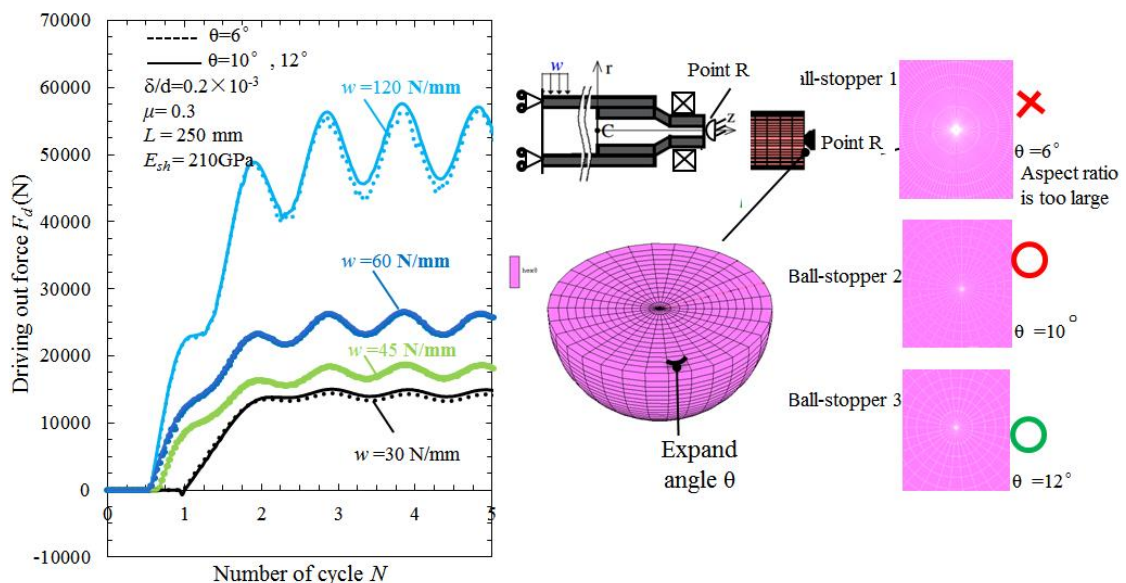
Figure 4.10 Driving out force F_d vs loading cycles N under fixed shrink fitting ratio $\delta/d=0.2 \times 10^{-3}$, friction coefficient $\mu= 0.3$, different loads and different Ball-stoppers

model along the same direction (the comging out z-direction) within 9 %. This indicates that the driving out mechanism of the three-dimentional real model is the same as the two-dimentional. That is the resultant frictional shear forces occurred on the shrink fitting surface when load is applied can be taken as the driving out force generated on the shaft.

Then, the coming out displacement reprented by Point C is also calculated out by the Ball-stopepr model 3 under the standard condition as is shown in Figure 4.11. Similar as the tendency of F_d (see Figure 4.10), the coming out displacement of Point C, Uzc increases at the begaining and stay stable after several cycles. Uzc is almost proportional to the load P when $P \le 60$N/mm but it increases greatly when doubles the laod ($P = 120$N/mm).

Table 4.3 Driving out force F_d and the frictional force $F_{\tau}^{resultant}$ at 3.9 cycle when the driving out force F_d become relatively stable at the peak position

	F_d (kN)	$F_{\tau}^{resultant}$ (kN)	Error
P = 30 N/mm	14.95	13.60	9.0%
P = 45 N/mm	18.76	17.22	8.2%
P = 60 N/mm	26.33	24.77	5.9%
P =120N/mm	55.71	50.97	8.5%

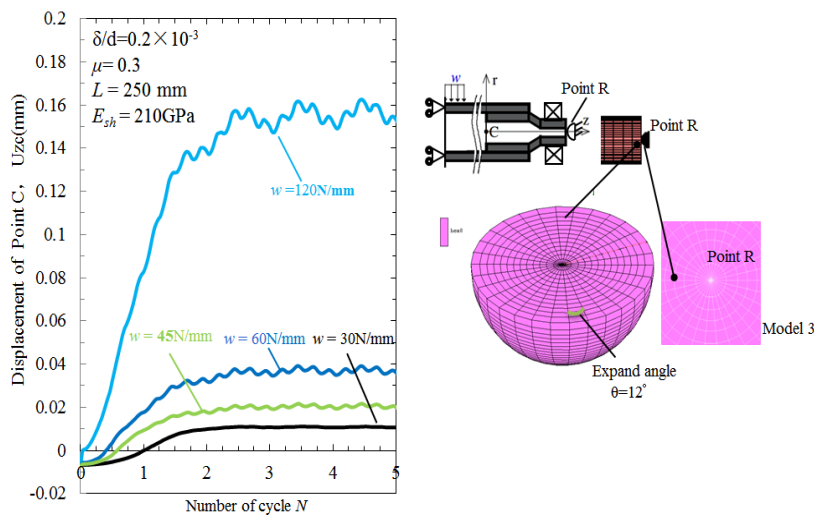Figure 4.11 The coming out displacement of Point C along z-direction vs loading cycles N under fixed shrink fitting ratio $\delta/d=0.2\times10^{-3}$, fixed friction coefficient $\mu= 0.3$ and different load

4.4 Conclusions

In this chapter, the actual three-dimensional model is considered to explore the coming out mechanism and to calculate the driving out force F_d^{3D}. Here, a novel Ball-stopper installed outside of the shaft designed for the three-dimensional model originally fertilising the analysis of the generation mechanism of driving out force F_d^{3D} and the calculation of F_d^{3D} is introduced. The function of this kind of Ball-stopper is firstly proved by comparing with the two-dimensional model with an inner stopper used in Chapter 2 and Chapter 3. Then the generation mechanism of driving out force F_d^{3D} is clarified and F_d^{3D} is calculated out with the help of the Ball-stopper.

(1)The driving out forces F_d firstly increase then become stable after several cycles due to the stopping work of the Ball-stopper. And the coming out displacements show similar tendency.

(2)The generation mechanism of the driving out force of the three-dimentional model is almost the same as the two-dimentional model.

(3)The resultant frictional shear forces occurred on the shrink fitting surface when load is applied can be taken as the driving out force generated on the shaft.

4.5 References of Chapter 4

[1] R. P. Larsen and A. D. Vyas: The Outlook for Ceramics in Heat Eegines: 1900-2010, SAE Paper No. 880514, Society of Automotive Engineers, Dearborn, MI, (1998).

[2] N.A. Noda, Hendra, M. Oosato, K. Suzumoto, Y. Takase, W. Li, Strength analysis for shrink fitting system used for ceramics rolls in the continuous pickling line, Key Eng. Mater. 462‑463 (2011) 1140‑1145.

[3] S. Matsuda, D. Suryadi, N.A. Noda, Y. Sano, Y. Takase, S. Harada : Trans. Jpn. Soc. Mech. Eng. A, 79(2013), 989.

[4] E. Ogawa, K. Shimizu, S. Hamayoshi, N. Kumagai, Y. Ohtsubo, N.A. Noda, Y. Takase, K, Kishi, K. Shobu, T. Tabaru, E, Maeda, S. Koga, T. Matsuda: Hitachi Metals Technical Review, 28(2012), 50.

[5] Noda,N.A.,Suryadi,D.,Kumasaki,S.,Sano,Y.,Takase,Y.:Failure analysis for coming out of shaft

from shink-fitted ceramic sleeve, Engi.Fail.Anal.,57(2015),219.

[6]   Sano,Y., Sakai,H., Zhang, G., and Noda, N.A.: Experimental verification of the coming out of the shaft for the ceramic rolls/rollers with shrink fitting system, 6th Int.Conf. on Fracture Fatigue and Wear, IOP Publishing, Bristol, (2017),012075.

[7]   C. E. Truman and J. D. Booker: Engineering Failure Analysis, 14 (2007), 557.

[8]   N. Antoni: Applied Mathematics and Mechanics, 37 (2003), 2352.

[9]   N.A. Noda, Y. Xu, Y. Sano, Y. Takase: ISIJ Int., 56(2016), No. 2, pp. 303–310.

[10] Marc Mentat team, Theory and User Information. Vol.A, MSC.Software, (2012) ,713.

[11] Marc Mentat team, Theory and User Information. Vol.A, MSC.Software, (2012) ,545.

Chapter 5 Conclusions

Ceramic sleeve rollers which can be used in steel manufacturing industries efficiently have been developed recently. Ceramics have high corrosion resistance, heat resistance and wear resistance. The ceramic cylinder and the steel shafts of both ends are joined together to form the ceramic sleeve roller. It is found that the shrink fitting method is the most suitable connecting method for the roller. However, since only small shrink fitting ratios can be applied due to the brittleness of the ceramics, coming out of the shaft from the sleeve happened during repeated loadings.

To find out the coming out mechanism of the shaft from the sleeve with less computational time in a much more understandable way, a two-dimensional simplified model with a newly introduced stopper is used to perform the coming out simulation. Then before analyzing the actual three-dimensional real model, it is useful to perform the analysis by a two-dimensional model. The effect of the shrink fitting ratio δ/d on the driving out force F_d of the shaft is discussed as well as several other parameters, such as the magnitude of the load P, the friction coefficient μ, shrink fitting ratio δ/d, shrink fitting length l, Young's modulus of the shaft E_{in}. Finally, it is necessary to explore the coming out mechanism and to calculate the driving out force F_d^{3D} for the actual three-dimensional model, and try to design the actual structure. Here, a novel Ball-stopper installed outside of the shaft designed for the three-dimensional model originally to fertilize the analysis of the driving out force F_d^{3D} mechanism and calculation of F_d^{3D} is introduced. The conclusions can be summarized in the following way.

1. For the simplified two-dimensional model with inner stopper, shear forces are generated along with the upside and downside at the fitting portions of the inner plate to balance the alternate bending load. The inner plate comes out gradually when the shear forces in the coming out direction exceeds the shear force in the opposite direction.

2. When the alternate loading is applied, the inner plate and the stopper come into contact with each other. The contact forces generated on the stopper can be regarded as the driving out forces.

3. In order to clarify the coming out phenomenon and generation mechanism by the

simplified two-dimensional model with inner stopper, the no-load intervals are introduced into the alternate bending loading cycle. As a result, it is found that the residual displacement appears during the no-loading interval. The coming out process can be explained in an easily understandable way by the accumulation of the residual displacements.

4. The effect of the friction coefficient μ on driving out force F_d is shown to exhibit the unique behavior as shown in Figure 3.2 by the simplified two-dimensional model with inner stopper. That is, as μ increases from $\mu = 0$, F_d gradually increases, but reaches a maximum value near $\mu = 0.45$ and then gradually decreases until $F_d = 0$.

5. The effect of the fitting ratio δ/d on driving out force F_d was shown to exhibit the unique behavior as shown in Figure 3.5 by the simplified two-dimensional model with inner stopper. That is, when δ/d is small, F_d takes an almost constant value, but when δ/d increases, F_d reaches a maximum value near δ/d = 0.3×10^{-3} and then sharply decreases to 0 near δ/d = 0.45×10^{-3}.

6. As shown in Figure 3.8, the effect of the fitting length ratio *l*/d on driving out force F_d is found to be different from the effects of the friction coefficient and the shrink fitting ratio by the simplified two-dimensional model with inner stopper. That is, when *l*/d increases from 0, it decreases rapidly and then keeps a constant value from around *l*/d = 0.2, but when *l*/d exceeds around 1.0, it starts to drop, near *l*/d = 1.6, F_d reaches to 0.

7. The effect of Young's modulus of the shaft E_{in} on driving out force F_d was shown to exhibit the unique behavior as shown in Figure 3.9 by the simplified two-dimensional model with inner stopper. That is, when E_{in} is small, F_d takes an almost constant value, but when δ/d increases, F_d reaches a maximum value near $E_{in} / E_{in}^{\text{standard}} = 1.5$ and sharply decreases to 0 near $E_{in} / E_{in}^{\text{standard}} = 3$.

8. When designing an actual three-dimensional roller, the maximum values of the driving out force F_d should be obtained based on the behavior clarified in conclusions 4~7 in Chapter 5, and used for the strength design of the structures for prevention of the coming out of the shaft. Thus, the knowledge obtained by this kind of two-dimensional models can be applied to the analysis of the

actual three-dimensional model.

9. For the analysis of the actual three-dimensional model in Chapter 4 as is shown in Figure 4.8, the driving out forces F_d^{3D} firstly increase then become stable after several cycles due to the stopping work of the Ball-stopper. And the coming out displacements show a similar tendency with the results obtained by the two-dimensional model (see Figure 2.4).

10. The generation mechanism of the driving out force F_d^{3D} for the three-dimensional real model is almost the same as the two-dimensional model. The resultant frictional shear forces $F_\tau^{resultant}$ occurred on the shrink fitting cylinder surface when the load is applied can be taken as the driving out force generated on the shaft. F_d^{3D} drives the shaft gradually coming out, which result in the failure of coming out of the shaft from the ceramic sleeve.

Appendix

Appendix A: Classification of advanced ceramic

Advanced ceramic such as alumina, aluminum nitride, zirconia, silicon carbide, silicon nitride and titania-based materials, each with their own specific characteristics, offer a high-performance, economic alternative to conventional materials such as glass, metals and plastics. Physical properties such as hardness, strength, wear resistance, corrosion resistance and thermal stability are considered while choosing a material. Each of these can be optimized depending on the choice of material. There are five important classes of advanced ceramic for large structure as follows [1].

1. Alumina ceramic (Al2O3)

Alumina Ceramic is the most widely used fine ceramic material. This material offers a combination of good mechanical and electrical properties such as high electrical insulation, high mechanical strength, high wear and chemical resistance. Its high dielectric properties are beneficial in electronic products. Alumina can be formed using several ceramic processing methods and can be processed machined or net-shaped to produce a variety of sizes and shapes. Furthermore it can be readily joined to other ceramics or metals using specially developed metallizing and brazing techniques.

Alumina ceramic is often classified into high alumina (80% alumina oxide) and porcelains (having less than 80% aluminum oxide). High aluminas are used in many mechanical devices and electronics. Strength and other properties generally improve as the percentage of alumina is increased.

2. Zirconia ceramic (ZrO2)

Zirconia oxide has the highest strength and toughness at room temperature of all the advanced ceramic materials. The fine grain size allows for extremely smooth surfaces and sharp edges. Zirconia offers corrosion and chemical resistance at high temperatures above the melting point of Alumina. Zirconia exist in three different crystal structures such as monolithic (stable at room temperature and become up to about 1400°C), tetragonal (stable up to 2370°C) and cubic. Three types of zirconia ceramic used in the technical applications are cubic, partially stabilized and

tetragonal zirconia. Cubic zirconia has low fracture toughness and strength. Partially stabilized zirconia (PSZ) has larger fracture toughness. Tetragonal zirconia has highest toughness and strength compared to cubic and partially stabilized zirconias.

3. Sialon ceramic (SiAlON)

SiAlONs are ceramic alloys based on the element silicon (Si), aluminium (Al), oxygen (O), and nitrogen (N) to solve the problem of silicon nitride (Si3N4) being difficult to fabricate. The combination of silicon nitride and aluminum oxide produces a material with the excellent strength, hardness, fracture toughness and low thermal expansion of silicon nitride, enhanced by corrosion resistance, good high temperature strength and oxidation resistance imparted by the aluminum oxide.

4. Silicon carbide ceramic (SiC)

Silicon carbide has the highest corrosion resistance of all the advanced ceramic materials. It also retains its strength at temperatures as high as 1400°C and offers excellent wear resistance and thermal shock resistance. Silicon carbide is formed in two ways, reaction bonding and sintering. The advantage of silicon carbide for reaction bonded is low cost, and the other side, silicon carbide for hot pressed is high strength but high cost for finished components, which is due to the difficulty in machining process. Advantage of sintered type is that most of the machining can be used easily.

Reaction bonded SiC is made by infiltrating compacts made of mixtures of SiC and carbon with liquid silicon. Sintered SiC is produced from pure SiC powder with non-oxide sintering aids. Conventional ceramic forming processes are used and the material is sintered in an inert atmosphere at temperatures up to 2000°C or higher.

5. Silicon nitride ceramic (Si3N4)

Silicon nitride ceramic is superior to other ceramic materials due to its thermal shock resistance. It also offers an excellent combination of low density, high strength, low thermal expansion and good corrosion resistance and fracture toughness. Silicon nitride ceramic is produced in two main ways; reaction bonded silicon nitride (RBSN), and hot pressed silicon nitride (HPSN) and sintered silicon nitride (SSN). RBSN is made by direct reacting

compacted silicon powder with nitrogen, and produces a relatively low-density product compared with hot pressed and sintered silicon nitride, however the process has only a small volume change allowing net shape forming. The HPSN and SSN material is made with sintering aids and offers better physical properties suitable for more demanding applications. Among non-oxide ceramic Si3N4 has been most widely studied based on its natural exhibit a potential up to temperature of 1,500℃[33]. In this present research, Si_3N_4 will be used.

Appendix

Appendix B : Mechanical and thermal properties of ceramic

Table A.1 shows the mechanical and thermal properties of ceramic [1]. Brief explanation on the properties of ceramic is provided as follows.

1. Hardness and elasticity

Hardness of ceramic is normally expressed by the size of the indent made by pressing a diamond indenter against the ceramic surface. When a solid is stressed (force/area), the solid is deformed in accordance with Hooke's law, which is expressed as (stress) = (elasticity) × (deformation). The elasticity (Young's modulus, E) is obtained by dividing the stress by the deformation (elongation/length). The hardness of material relates to resistance of material to abrasive wear.

Table A.1 Mechanical and physical properties of advanced structural ceramic [1]

Material	Density (g/cm3)	Flexural strength (MPa)	Fracture Toughness (MP.m1/2)	Elastic Modulus (Gpa)	Poisson's ratio	Hardness (Gpa)	Thermal Expansion coefficient (1/K)	Thermal conductivity (W/mk)
Silicon nitride								
Sintered	3.2	600	4.5	276	0.24	14	3.4	28
Hot pressed	3.2	800	5.0	317	0.28	20	3.2	30
Reaction bonded	2.5	210	3.6	165	0.22	10	2.8	6
Sintered reaction bonded	3.3	825	-	297	0.28	19	3.5	30
HIPed	3.2	1000	6.0	310	0.28	20	3.5	32
Sialon	3.2	650	5.0	297	0.28	18	3.2	22
Silicon carbide								
Hot pressed	3.2	550	3.9	449	0.19	25	4.5	70
Sintered	3.1	400	3.0	427	0.19	27	4.8	80
Reaction bonded	3.0	350	3.5	385	0.19	17	4.4	90
CVD	3.2	500	2.6	450	-	30	5.5	150
Alumina(%)								
85	3.4	296	3.5	221	0.22	10	5.3	15
90	3.6	338	3.5	276	0.22	11	6.1	17
96	3.7	352	4.5	303	0.21	12	6.3	23
99.8	3.9	552	4.5	386	0.22	15	7.1	30
Zirconia								
Cubic	5.9	245	2.4	150	0.25	11	8.0	1.7
TZP	6.1	1020	11.0	210	0.24	13	10.6	0.4
PSZ	6.0	750	8.1	205	0.23	12	8.3	2.1

Appendix

Because of their high hardness, ceramic is suitable for application requiring resistance to abrasive and erosive wear.

2. Strength

The theoretical strength of a material is expressed by the force required to separate the atoms that constitute the material. The strength of ceramic intended for structural materials ranges from 400 to 800 MPa. The actual strength of materials is lower than the expected values because the stress is concentrated at defects (cracks) inside the material. The strength decreases as the size of the defect increases. Defect sizes are statistically distributed in materials. Therefore, the strength of a material varies and is evaluated statistically (Weibull distribution). The strength of a material is expressed accurately by the mean value or the Weibull distribution function obtained by testing many samples to failure. The strength is classified into bending strength, tensile strength, and compressive strength, which are measured by different methods.

3. Fracture toughness

Materials contain defects (cracks) and the material fracture is caused by the stress concentrated at the tip of a crack. The value of the stress concentration is expressed by the stress intensity factor K. The crack starts to extend rapidly, leading to breakage, when K reaches a certain value. The value at this point is the critical stress intensity factor or the fracture toughness value K_C, which expresses the toughness (or fragility) of the material. Stress at this point is the fracture strength (strength) of the material. Strength depends on the length and shape of the crack as well as the fracture toughness value.

4. Specific heat capacity

A solid material, when heated, experiences an increase in temperature signifying that some energy has been absorbed. The summation rules of specific heat capacities of oxides are applicable in an approximate sense to multiple oxides over a wide range of temperatures while not being limited to high temperatures. In actual materials, thermal changes due to property changes such as thermal vibration, defect formation, electron thermal excitation and phase transition properties affect the change in heat capacity, and therefore, precise measurements and analyses are performed.

5. Thermal expansion.

The expansion of substances responding to temperature change is characterized by the coefficient

of thermal expansion. When an interatomic potential develops in a material becomes asymmetric, thermal expansion occurs responding to the temperature increase. Ceramic materials that are to be subjected to temperature changes must have coefficients of thermal expansion that are relatively low, and in addition, isotropic. Otherwise, these brittle materials may experience fracture as a consequence of non-uniform dimensional changes in what is termed thermal shock. When various components consisting of difference materials are subject to changes in temperature, design specifics need to be considered due to differences in thermal expansion.

6. Thermal conductivity

Thermal conductivity values for a number of ceramic materials range between approximately 2 and 50W/m-K. Porosity in ceramic materials may have a dramatic influence on thermal conductivity; increasing the pore volume will, under most circumstances, result in a reduction of the thermal conductivity. In fact, many ceramics that are used for thermal insulation are porous. Heat transfer across pores is ordinarily slow and inefficient. Internal pores normally contain still air, which has an extremely low thermal conductivity—approximately 0.02 W/m-K.

Reference of Appendix

[1]. Ogawa, Y., Ogasawara, T., Machida, M., Tsukawaki, Y. et al., Complete Ceramic Swirl Chamber for Passenger Car Diesel Engine, SAE Technical Paper 870650, 1987